2017

Experimental Investigation of a Parametric Excitation of Whistler Waves

Nathan E. Zechar
Wright State University

Repository Citation

Zechar, Nathan E., "Experimental Investigation of a Parametric Excitation of Whistler Waves" (2017). *Browse all Theses and Dissertations*. 1773.
https://corescholar.libraries.wright.edu/etd_all/1773

EXPERIMENTAL INVESTIGATION OF A PARAMETRIC EXCITATION OF WHISTLER WAVES

A thesis submitted in partial fulfillment
of the requirements for the degree of
Master of Science

By

Nathan E. Zechar
B.S., Wright State University, 2014

2017
Wright State University

WRIGHT STATE UNIVERSITY

GRADUATE SCHOOL

April 29, 2017

I HEREBY RECOMMEND THAT THE THESIS PREPARED UNDER MY SUPERVISION BY Nathan E. Zechar ENTITLED Experimental Investigation of the Parametric Excitation of Whistler Waves BE ACCEPTED IN PARTIAL FULFILLMENT OF THE REQUIREMENTS FOR THE DEGREE OF Master of Science

Amit Sharma, Ph.D.
Thesis Director

Jason Deibel, Ph.D.
Chair, Department of Physics

Committee on
Final Examination

Amit Sharma, Ph.D.

Jerry Clark, Ph.D.

Vladimir Sotnikov, Ph.D.

Robert E.W.Fyffe, Ph.D.
Vice President for Research and
Dean of the Graduate School

ABSTRACT

Zechar, Nathan E. M.S., Department of Physics, Wright State University, 2017.
Experimental Investigation of the Parametric Excitation of Whistler Waves.

Previous theoretical work has shown that a parametric interaction between electrostatic lower oblique resonance (LOR) and ion acoustic waves (IAW) can produce electromagnetic whistler waves in a cold magnetized plasma. It was also demonstrated theoretically that this interaction can more efficiently generate electromagnetic whistler waves than by direct excitation using a conventional loop antenna. For the purpose of experimentally validating the above result, an experimental facility was designed and constructed utilizing a vacuum chamber, electromagnets, and a helicon plasma source array capable of producing a volume of plasma with high density and spatial uniformity. Additionally, positioning equipment and plasma diagnostics such as an RF compensated

Langmuir probe and electrostatically shielded Bdot probes were fabricated to capture plasma parameter and time varying magnetic field data. The ability to experimentally excite the LOR, whistler wave, and IAW was demonstrated by utilizing the fabricated diagnostics. This data was then arranged to display spatial wave topologies which agreed with each wave’s respective dispersion relation.

Finally the parametric antenna was implemented to produce whistler waves through the interaction of LOW and IAW waves. The spatial and temporal information of the frequency components of these waves were analyzed by applying a band pass filter via Fourier analysis.

TABLE OF CONTENTS

LIST OF FIGURES

LIST OF TABLES

ACKNOWLEDGMENTS

I would like to thank Dr.Vladimir Sotnikov, the theoretical physicist and head of the plasma physics sensors laboratory (PPSL) at AFRL. Without his previous theoretical legwork, these efforts would not have been possible. Dr.Sotnikov was my professor for my graduate plasma physics course and my boss throughout my time with the PPSL group. I express extreme gratitude towards Dr. Manuel Urrutia for his patience while offering his consulting expertise in experimental technique. I am grateful for my coworkers Dr. Mark Hopkins, Dr. Chris Plechaty, and James Caplinger for expediting my familiarity and competence of laboratory instrumentation and analytical software. I am thankful for Dr.Clark taking the time to help me prepare my thesis. I am extremely appreciative of Riverside Research and Tony Kim of AFRL for selecting me to be a member of the PPSL team. Last and most importantly, I want to praise my parents for providing me with a strong foundation through their hard work and educational support. My accomplishments are a product of their never-ending generosity.

1 Introduction

1.1 Radiation Belt Remediation

The focus of this research is to test the usability of a novel parametric antenna as a device for the generation of very low frequency (VLF) waves in ionospheric/space plasmas. Realization of this technology has the potential to reduce the energy consumed to generate whistler waves by antenna excitation aboard space assets. This will increase the effectiveness of radiation belt remediation via very low frequency wave excitation and in general act to safeguard space assets.

Natural and artificial Radiation Belts (RB) are hazardous to spacecraft due to highly energetic particles which have the potential of causing serious damage to onboard electronics. A High Altitude Nuclear Detonation (HAND) induced radiation belt can destroy 90% of low Earth orbit (LEO) satellites within months. Similar phenomenon take place naturally during magnetic storms caused by enhanced solar activity. Radiation belt remediation (RBR) is aimed at significantly reducing highly energetic particles in the ionosphere that are harmful to satellite electronics. Very Low Frequency (VLF) waves, known as whistler waves, injected from low Earth orbit (LEO) satellites into the magnetosphere can significantly reduce to presence of highly energetic charged particles arising from HAND devices or solar flares.

1.2 The Parametric Antenna

The lifetime and reliability of space systems is often limited by the steady degradation caused by these particles. This can be mitigated by implementation of the radiation belt remediation (RBR) technology which reduces the life time of the energetic particles with high power VLF whistler waves injected into the magnetosphere from LEO satellites. Figure 1.2.1-*a, shows* a radiation belt resulting from a high altitude nuclear detonation (HAND), while Figure 1.2.1-*b* demonstrates the remediation process utilizing VLF waves.

The main challenge in this approach is, however, to design a viable antenna that efficiently radiates in the electromagnetic (EM) portion of the VLF spectrum. The main deficiency of current space-born VLF antennas shown through several research efforts [1], [2], [3], [4], [5], [6], [7] is that only a small portion (less than 3%) of the radiated field goes directly into the whistler mode, thus dramatically limiting the effective range of RBR. Since the 1980s, VLF scattering has been recognized as the best approach to accomplish RBR. However, realization of this approach has been limited by inefficient antenna designs.

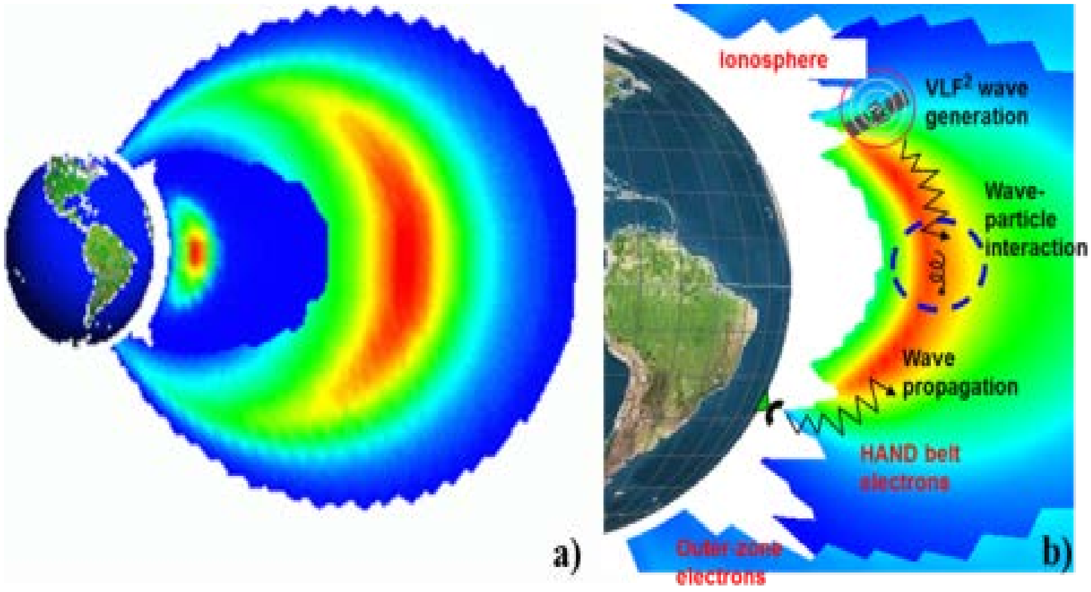

Figure 1.2.1 - *a) HAND belt (red), b) Illustration of RBR mechanism*

Dr. Sotnikov of AFRL had proposed a revolutionary approach to improve efficiencies from about 3% to 50% or better, and make space based VLF antennas a reality. One investigated approach utilized a loop antenna and a dipole antenna transmitting at different frequencies. Their combined use interacts with the non-linear plasma in the ionosphere, creating a region in the plasma that acts like a much larger antenna, re-radiating the VLF energy which generates higher magnitude whistler waves when compared to a conventional loop antenna.

Radiation properties of VLF loop antennas in the ionosphere were investigated during the preparation phase of the International Space Project [8]. Fisher and Gould have shown for the VLF frequency range, for a given frequency, both quasi-electrostatic and electromagnetic components in the VLF wave spectrum can be excited [9], [10]. Quasi-electrostatic components of an excited wave spectrum are called Low Oblique Resonance (LOR) oscillations while the other component is an electromagnetic (EM) whistler wave.

2 Theory

2.1 Parametric Excitation of Whistler Waves: Theory

In this section, we will analyze excitation of waves with frequencies ω several times above the lower hybrid resonance frequency (ω_{LH}), but below the electron cyclotron frequency (ω_{ce}) i.e.

$$\omega_{LH} < \omega < \omega_{ce} \tag{2.1.1}$$

where ω_{LH} is given by:

$$\omega_{LH} = ((\omega_{CE}\omega_{CI})^{-1} + \omega_{PI}{}^{-2})^{-1/2} \tag{2.1.2}$$

ω_{ce} is the electron cyclotron frequency, ω_{pe} and ω_{pi} are the electron and ion plasma frequencies given by

$$\omega_{CE} = \frac{q|B|}{m_e c} \tag{2.1.3}$$

$$\omega_{PI} = \sqrt{\frac{4\pi Z^2 q^2 n_i}{m_i}} \qquad (2.1.4)$$

Where q is the fundamental charge, $|B|$ is the magnitude of the magnetic field, m_e is the mass of an electron, m_i is the mass of the ion species, Z is the number of protons of the ion species, c is the speed of light, n_e is the number of electrons per cubic centimeter, and n_i is the number of ions per cubic centimeter.

Linear excitation of VLF waves by a loop antenna has been extensively studied in other experimental research efforts [9] - [11]. Under the conditions shown in equation (2.1.1) only one mode is excited in cold plasmas. A main feature of the radiation far away from the source can be understood from the plot analogous of wave refractive index surface. This plot can be obtained using the expression for the dispersion of VLF waves:

$$\omega^2 = \frac{\omega_{LH}^2}{\left(1 + \omega_{pe}^2/k^2c^2\right)^2}\frac{m_i}{m_e}\frac{k_z^2}{k^2} \qquad (2.1.5)$$

$$\omega_{PE} = \sqrt{\frac{4\pi q^2 n_e}{m_e}} \qquad (2.1.6)$$

In equation (2.1.5), k_z is the wave vector component along the magnetic field and $k_\perp$is the perpendicular component. By schematically plotting the wave vector component k_z against $k_\perp$ for a given ω one can obtain the plot shown in

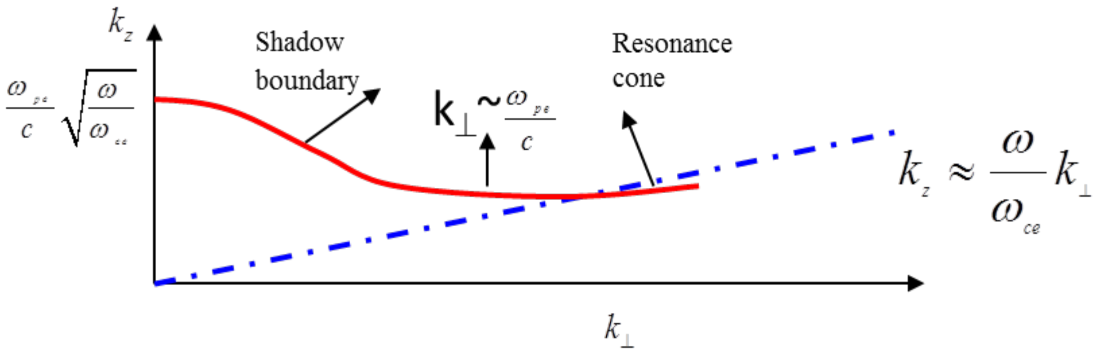

Figure 2.1.1- *Wave number surface for constant angular frequency with conditions:* $\omega_{LH} < \omega < \omega_{ce}$ *with three critical points*

A great deal of the source power is radiated as a quasi-electrostatic (LOR) wave as shown in "Radiation and Scattering of Waves" [3] with $\omega_{pe}^2/k^2c^2 \ll 1$. The real electromagnetic mode, the whistler wave, with $\omega_{pe}^2/k^2c^2 \ll 1$ is radiated in oblique directions up to an angle ~ 19.5^0, which is the shadow boundary determined by the long wavelength inflexion point and these waves are radiated comparatively weak. For many ionospheric applications, it is important to increase the level of the radiated power which is going into the electromagnetic part of the excited wave spectrum which is the whistler wave.

Below we will analyze the efficiency of a parametric mechanism of transformation of quasi-electrostatic LOR waves excited by a loop antenna operating at frequency ω on density perturbations produced by a dipole antenna (low frequency source) with frequency Ω which excites ion-acoustic waves with frequency above the ion cyclotron frequency but well below the lower hybrid frequency. In this case whistlers will be excited on combination frequencies $\omega \pm \Omega$. The dipole is placed in the center of the loop and lies in its plane. Such an arrangement may be regarded as a parametric antenna for enhanced excitation of whistlers.

2.2 Excitation of VLF waves by a loop antenna

This section discusses the distribution of an electric field excited by a loop antenna, the total radiated power, and, power radiated into the electromagnetic part of the whistler wave spectrum. We will briefly discuss the cases when a loop plane is perpendicular the direction of the ambient magnetic field. We will also calculate total radiated power and portion of radiation that goes directly into excited electromagnetic part of the VLF wave spectrum – whistler waves, for the case when a loop plane is parallel to an external magnetic field. This is important especially for active experiments in the ionosphere since whistler waves can propagate a great distance from the source region.

Logarithmic type singularities along the resonance cones are displayed when the plane of a loop is perpendicular to an external magnetic field which was previously shown by Wang et al and Sotnikov [11]- [12]. This is schematically represented in Figure 2.2.1

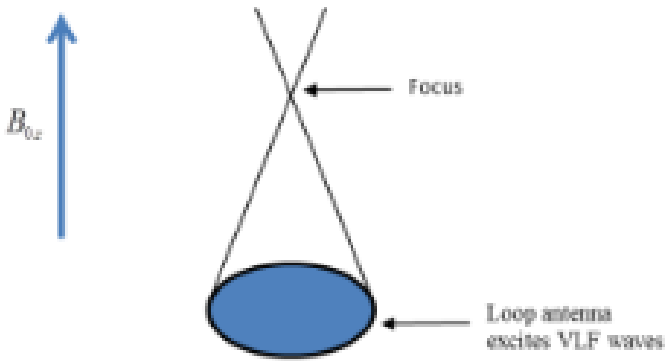

Figure 2.2.1 *Resonance surfaces of a loop antenna. On these surfaces, the wave potential experiences logarithmic type singularity.*

In another case, when magnetic field lies in a loop plane shown in Figure 2.2.2 there are two resonance surfaces, one inside the other. The method of obtaining these surfaces was suggested in [9].

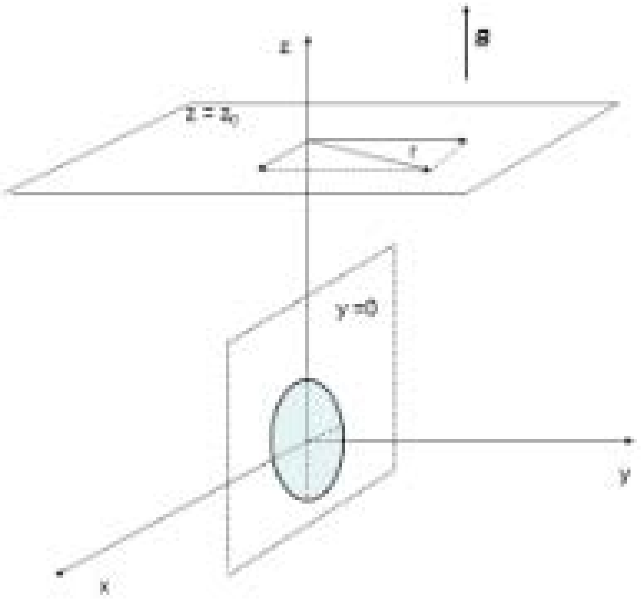

Figure 2.2.2 *The coordinate system used. The loop antenna is in the y=0 plane and an external magnetic field is along the z axis.*

Internal and external resonance surfaces are plotted below, in *Figure 2.2.3*. On these surfaces, excited field experiences logarithmic type singularities.

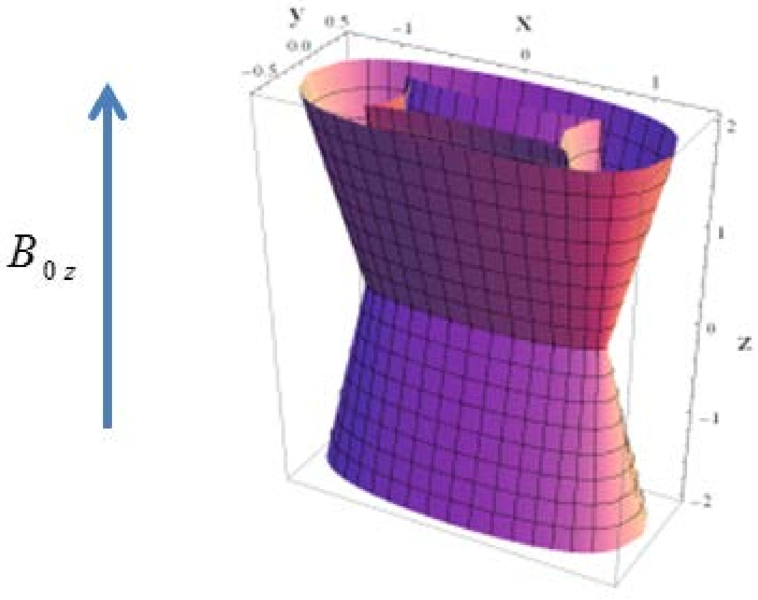

Figure 2.2.3 *Example of two resonance surfaces internal and external of a loop antenna with an external magnetic field in a loop plane.*

In order to calculate total radiated power and power which goes to the electromagnetic part of the VLF wave spectrum for whistler waves, we consider a time harmonic loop current source, $I_0\ exp(j\omega t)$, and begin with the expression for the radiated power as shown by Fisher and Gould [9]:

$$P = -\frac{1}{2} Re \int \boldsymbol{J}_m(\boldsymbol{r}) \cdot \boldsymbol{H}^*(\boldsymbol{r}) d^3 r = -4\pi^3 Re \int \boldsymbol{m}(\boldsymbol{k}) \cdot \boldsymbol{H}^*(\boldsymbol{k}) d^3 k \qquad (2.2.1)$$

Where $\boldsymbol{m}(\boldsymbol{k})$ and $\boldsymbol{H}(\boldsymbol{k})$ are Fourier components of the external magnetization and the magnetic induction created by this current. The asterisk denotes the complex conjugate. A different expression for radiated power using current in a loop antenna and the electric field created by this current was used by Wang and Bell [11].

Taking proper account of the resonance denominator found in Eq. (63) of "Resonance Cones in the Field Pattern of a Radio Frequency Probe in a Warm Anisotropic Plasma" [9], calculations were carried out for the following set of plasma parameters which correspond to ionospheric conditions: for an electron density of $n_e = 3 \times 10^4 cm^{-3}$ and for a background magnetic field of $B_0 = 0.3\ Gauss$.

The value of the current in a loop antenna was $I_0 = 100\ Amperes$ and the frequency was $\omega = 6 \times 10^4 rad\ s^{-1}$. The results in Figure 2.2.4(a) shows the total radiated power as a function of the angle between the antenna normal and the magnetic field. Figure 2.2.4(b) shows the long wavelength radiated power found by integrating in $k_\perp$ out to $\delta = k_\perp c/\omega_{pe} = 0.1$. These results were checked by performing the calculations using the spherical coordinate formulation used by Wang and Bell [11]. In all cases, we obtained agreement of the order of 0.1% or better, giving us confidence in the numerical methods used in our work.

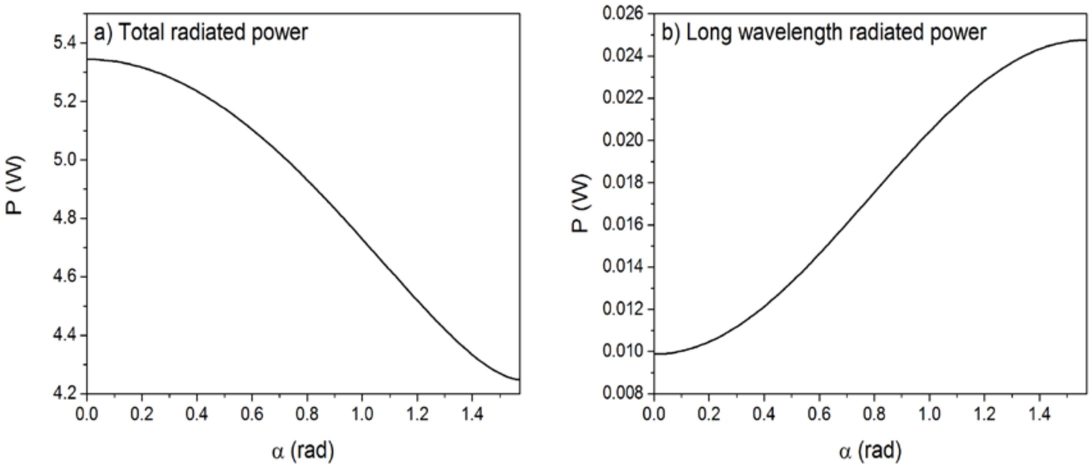

Figure 2.2.4- *(a) Total radiated power versus angle between the antenna loop normal and the magnetic field. (b) Radiated power at long wavelength (δ≤0.1) versus angle between the antenna normal and the magnetic field.*

2.3 Parametric excitation of electromagnetic whistler waves

The equation for analysis of nonlinear interaction of VLF waves with ion-acoustic (IA) waves in a magnetized plasma were derived by Birdsall et al [13]. Electric and magnetic fields in a magnetosonic type VLF wave were represented through a scalar potential φ and a vector potential $\mathbf{A}$ with the Coulomb gauge,

$$\boldsymbol{E} = -\nabla\varphi - \frac{1}{c}\frac{\partial \boldsymbol{A}}{\partial t} \tag{2.3.1}$$

and $\boldsymbol{B} = \nabla \times \boldsymbol{A}$ with $\nabla \cdot \boldsymbol{B} = 0$. For analysis of parametric excitation of electromagnetic whistler waves due to transformation of LOR waves with frequency ω excited by a loop antenna, on IA oscillations excited by another low frequency source with frequency Ω $(\omega_{ci} \ll \Omega \ll \omega)$ we can modify the equation derived by Sagdeev and Sotnikov [14].

Whistlers are excited on combination frequencies $\omega_{\pm} = \omega \pm \Omega$, and we are interested in the excitation of whistlers on frequencies from the range $\omega_{\pm} \sim (3-6)\omega_{LH}$. Sotnikov modified the equation from his previous works [15] [14] to write the parametrically excited whistler wave's Fourier component potential φ_{k_-} with $\omega_- = \omega - \Omega$ and $\boldsymbol{k}_- = \boldsymbol{k} - \boldsymbol{k}_s$:

$$\frac{\partial^2}{\partial t^2}\varphi_{NL}^t + \frac{c^4}{\omega_{pe}^2}\Delta\frac{\partial^2}{\partial {k_z}^2}\varphi_{NL}^t = -\frac{1}{n_0}\frac{1}{\omega_{ce}}\frac{\omega_{pe}^2}{c^2}\frac{\partial}{\partial t}[\nabla\delta n_s^*, \nabla\varphi^l] \qquad (2.3.2)$$

In equation (2.3.2) φ_{NL}^t is the potential associated with a parametrically excited whistler mode, φ^l is the potential of LOR mode excited by a loop antenna and δn_s is ion-acoustic type density perturbation excited by a dipole antenna. Equation (2.3.2) can be used to analyze the generation of whistlers due to parametric interaction of LOR waves with low frequency ion-acoustic type density perturbations excited by a dipole antenna. Using previously obtained expressions for φ^l and δn_s for the case when an external magnetic field is perpendicular to the loop plane, we arrive to the following expression for components of the electric field in the plane perpendicular to an external magnetic field:

$$E_{x,NL}^t = -\frac{1}{12\sqrt{2}}\frac{1}{en_0}\frac{\omega\omega_-\Omega^2\omega_{pe}^2}{\omega_{ce}c^4V_s^3}R_a^2 d_0 J_a J_d \frac{sin\phi}{r}\left(isin\phi - \frac{z}{r}cos\phi\right) \qquad (2.3.3)$$

$$E_{y,NL}^t = -\frac{1}{12\sqrt{2}}\frac{1}{en_0}\frac{\omega\omega_-\Omega^2\omega_{pe}^2}{\omega_{ce}c^4V_s^3}R_a^2 d_0 J_a J_d \frac{sin\phi}{r}\left(-icos\phi - \frac{z}{r}sin\phi\right) \qquad (2.3.4)$$

Knowledge of parametrically excited electric fields in a whistler mode allows us to proceed with the calculation of power radiated by parametrically excited nonlinear current$\boldsymbol{J}_{NL}(\boldsymbol{r},t)$:

$$\boldsymbol{J}_{NL}(\boldsymbol{r},t) = -e\delta n_s\boldsymbol{V}_{LOR} \tag{2.3.5}$$

In equation (2.3.5) $\delta n_s$is the ion-acoustic type density perturbation excited by a low frequency dipole and $\boldsymbol{V}_{LOR}$ is the speed of electrons in the presence of LOR wave excited by a loop antenna. To find δn_s we can use equation for excitation of ion-acoustic waves by a dipole antenna. In the simplest case of a point dipole antenna with the current density in the dipole given by $\delta\mathbf{j}_c = J_d d_0\delta(\mathbf{r})\mathbf{e}_x$ we have:

$$\delta n_s(x,y,z,t) = \frac{J_a d_0\Omega}{4\pi e V_s^2}\frac{x}{R^3}\left(i - \frac{\Omega R}{V_s}\right) exp\{i[\Omega(t - R/V_s)]\} \tag{2.3.6}$$

where $R = \sqrt{x^2 + y^2 + z^2}$. To find velocity $\boldsymbol{V}_{LOR}$which appears due to the presence of an electric LOR wave field excited by a loop antenna we can use the electron equation of motion in a drift approximation. Resulting expressions for $\boldsymbol{V}_{LOR}$ are:

$$\boldsymbol{V}_{LOR} = c\frac{\boldsymbol{E}_{LOR} \times \boldsymbol{B}_0}{B_0^2} \tag{2.3.7}$$

where $\boldsymbol{E}_{LOR}$ is the field of quasi-electrostatic LOR waves excited by a loop antenna. Now the expression for the radiated power of parametrically excited whistler waves can be written as:

$$P_{NL} = -\frac{1}{2} Re \int \boldsymbol{J}_{NL}^{*}(\boldsymbol{r}) \cdot \boldsymbol{E}_{NL}(\boldsymbol{r}) d^3 r \tag{2.3.8}$$

Using the same set of plasma parameters found in Kulkarni et al's works [16] one can obtain the value of power radiated into an electromagnetic part of VLF wave spectrum – whistler waves. Taking the current in a low frequency dipole antenna $J_d = 2\ A$, the value of radiated power for the case when the loop plane is perpendicular to an external magnetic field is $P_{NL} = 0.03\ W$. The value of radiated power (at the angle $\alpha = 0$) of a single loop antenna can be found to be $P_L = 0.01\ W$. Increasing the current in a dipole antenna to $J_d = 10$ for parametrically excited radiated power we have $P_{NL} = 0.6\ W$. These examples shows that parametric mechanism of excitation is very effective and produces much higher radiated power output in electromagnetic part of the VLF wave spectrum.

3 Plasma Wave Parameters

To engineer an experimental environment to observe the interaction of whistler waves and ion acoustic waves, one must consider the parameters of these waves and what factors give rise to these parameters. Wavelengths associated with electromagnetic and electrostatic plasma waves remain one of the most important guiding factors when considering the plasma chamber dimensions needed to observe wave phenomenon and house necessary instrumentation. The parameters of the expected plasma wave wavelengths used to guide the construction of experimental facility are explained below.

3.1 Whistler Waves

Plasma parameters used to calculate the wavelength of the electromagnetic portion of a whistler wave are described in the Appleton-Hartree dispersion relationship shown by Balkey [17]. This relationship describes N, the index of refraction of a whistler wave as a function of several plasma parameters and the whistler wave frequency to be excited with a loop antenna.

These parameters are $(\omega_A\ , \omega_{CE}, \omega_{PE}, \phi)$ where ω_A is the angular whistler wave frequency of the exciting antenna, ω_{CE} is the angular electron cyclotron frequency, ω_{PE} is the angular plasma frequency, and ϕ is the angle of whistler wave propagation with respect to the ambient background magnetic field where $\vec{k} \parallel \vec{B}_Z \ \Rightarrow \ \phi = 0$

$$N^2 = 1 - \frac{\omega_{PE}^2}{(\omega_A^2 - \omega_A \omega_{CE} \cos\phi)} \tag{3.1.1}$$

Evaluating equation (3.1.1) to show how the index of refraction affects wavelength in equation (3.1.2), it can be shown $\lambda_{Whistler}$ shortens as ω_{PE} increases and as ω_A approaches ω_{CE}.

$$\lambda(N)_{Whistler} = \frac{c}{fN} = \lambda_{VLF} \tag{3.1.2}$$

The parameters of the experimental setup can be tailored to allow several periods of the wavelength $\lambda_{Whistler}$ to fit inside a plasma chamber with given chamber dimensions. With the VLF antenna frequency set to $\omega_A = \omega_{VLF} = 2\pi f_{VLF}$, an upper limit for ω_{PE} and ω_{CE} can be chosen to determine $\lambda_{Whistler}$.

The parameter ω_{PE} is a function the of electron plasma density n_e shown in equation (2.1.3) which can be found in the NRL plasma formulary [18]. Considering equations (3.1.1) & (3.1.2), it can be shown a higher electron plasma density yields a shorter $\lambda_{Whistler}$. A shorter $\lambda_{Whistler}$ will require less axial chamber length to accommodate several $\lambda_{Whistler}$ within the chamber.

To achieve sufficient n_e, a suitable plasma source will need to be implemented. Helicon plasma sources are a well-studied and prove relatively easy to construct. These sources can efficiently generate plasma densities up to $n_e = 1e13\ cm^{-3}$ as previously shown by Balkey [17] and Chen [19].

Choosing $n_e = 1e11\ cm^{-3}$ as a modest achievable density for such a source, ω_{PE} is found to be $1.78e10\ rad \cdot s^{-1}$ for the upper limit when calculating an expected $\lambda_{Whistler}$.

The parameters ω_{CE} is a function of the background ambient magnetic field $\vec{B}_Z$ which can be found in the NRL plasma formulary [18]. Electromagnets will produce this magnetic field with the field component directed down the plasma chamber axis noted as the $\vec{Z}$ direction. A value for ω_{CE} can be estimated when considering the theoretical conditions in equation (3.1.3) which are needed for ion acoustic and whistler wave interaction.

$$\omega_{IA} < \omega_{LH} < \omega_{VLF} < \frac{1}{2}\omega_{CE} \ll \omega_{PE} \tag{3.1.3}$$

With $n_e = 1e11\ cm^{-3}$ chosen as the upper limit of the plasma density and setting $\omega_{CE} = .05\omega_{PE}$, we arrive to $\vec{B}_Z = 50\ Gauss$ as a background magnetic field which fits within the parameters of equation (3.1.3).

Because $\lambda_{Whistler}$ becomes small as $\omega_{VLF} \Rightarrow \omega_{CE}$, choosing $\omega_{VLF} = .5\omega_{CE}$ will give us the shortest possible wavelength within the theoretical parameters. Figure *3.1.1* displays $\lambda_{Whistler}(\emptyset_{B_z})$. The parameters associated with Figure *3.1.1* are shown below it.

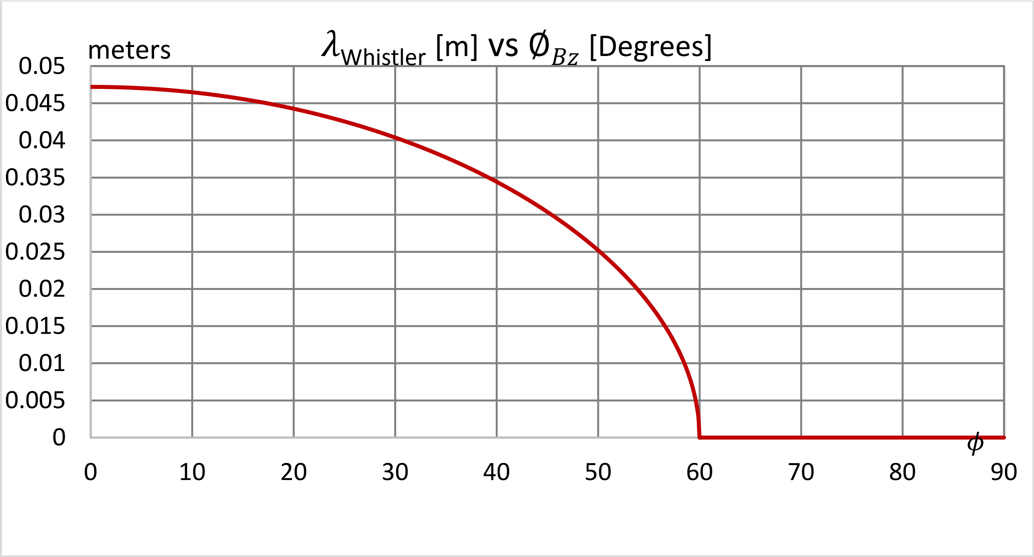

Figure 3.1.1 - *Whistler wavelength as a function of angle normal to B_z*

$$n_e = 1e11\ cm^{-3} \quad \Longrightarrow \quad \omega_{PE} = 1.78e10\ rad \cdot s^{-1}$$

$$\vec{B}_z = 50\ Gauss \quad \Longrightarrow \quad \omega_{CE} = 8.79e8\ rad \cdot s^{-1}$$

$$\omega_{VLF} = \frac{1}{2}\omega_{CE} \quad \Longrightarrow \quad f_{Antenna} = 70\ MHz$$

A cylindrical chamber with an axial length of 100cm will allow several periods of $\lambda_{Whistler} = 5cm$ or slightly longer to fit within the chamber. This length will also leave room within the chamber to accommodate diagnostic and positioning equipment for acquiring experimental data.

3.2 Lower Oblique Resonance

The plasma chamber dimensions will not be solely based on $\lambda_{Whistler}$. Chamber width is heavily dependent on the propagating width of the expected resonance cone to be emitted from the exciting loop antenna. Furthermore, chamber width must be selected to allow for diagnostic equipment design and ease of mechanical working space.

The electrostatic resonance cone is an integral component to the parametric antenna theory. The angle of this electrostatic portion of a whistler wave emits from a loop antenna as a function of the same parameters as that for the electromagnetic portion. Eq. (3.2.1) describes this angle as a function of several parameters which can be found in the experimental work of Fisher and Gould [9]. Considering the parameters chosen for the plasma environment above and plugging them into equation (3.2.1) we arrive at an angle of 21°.

$$\sin^2 \emptyset = \frac{{\omega_{VLF}}^2({\omega_{PE}}^2 + {\omega_{CE}}^2 - {\omega_{VLF}}^2)}{({\omega_{PE}}^2{\omega_{CE}}^2)} \tag{3.2.1}$$

Using a loop antenna with a diameter of 5cm and attempting to resolve at least 10 lengths of the calculated $\lambda_{Whistler}$, a chamber diameter of 50cm gives the required space needed as illustrated in Figure *3.2.1*. The selected chamber width and diameter should also prove enough room to allow for diagnostic devices and positioning equipment to rest inside of the chamber.

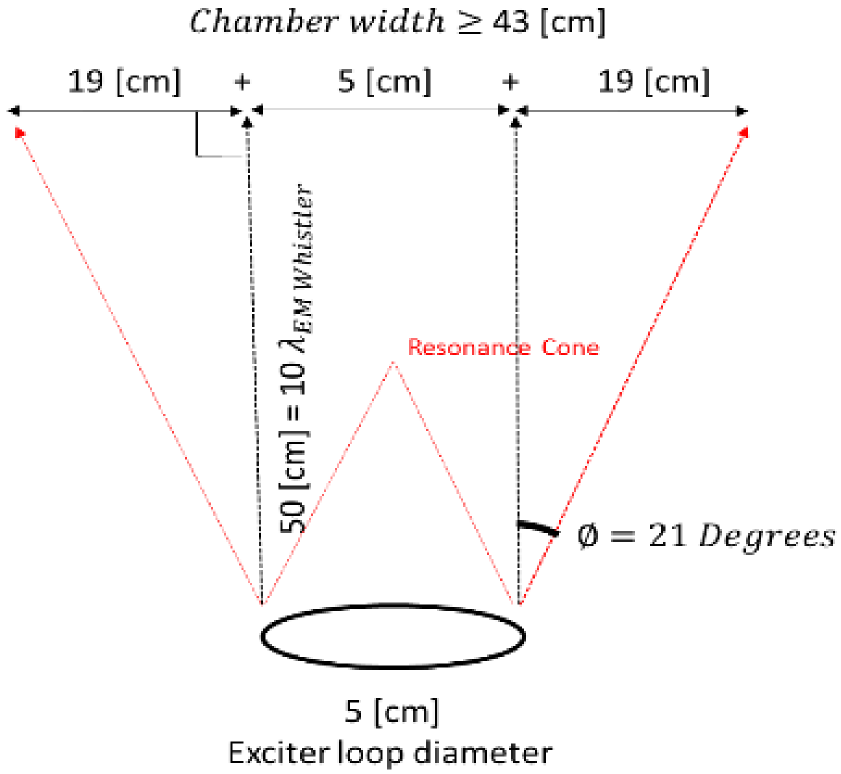

Figure *3.2.1 - Resonance cone angle. Not to scale.*

3.3 Ion Acoustic Waves

Before finalizing the plasma chamber dimensions, the ion acoustic wavelength should also be evaluated to ensure several periods of the plasma wave will fit inside the plasma chamber.

In order to determine the wavelength of an ion acoustic wave, the ion acoustic sound speed must be considered. The sound speed is shown in the works by Gekelman et al [20]. Evaluating equation (3.3.1) helps perceive this relationship. The units of c_s are in $cm \cdot s^{-1}$.

$$c_s = \sqrt{\frac{\gamma_e Z K_B T_{e+} \gamma_i K_B T_i}{M}} \tag{3.3.1}$$

(3.3.1) can be approximated for plasma conditions where; the electron temperature T_e is much greater than the ion temperature T_i, the plasma is a singly ionized species, and for ion acoustic frequencies lower than the ion plasma frequency (ω_{PI}). The approximation is shown in equation (3.3.2).

$$c_s = 9.8e8\sqrt{\frac{T_e}{m_i}} \tag{3.3.2}$$

Approaching ion acoustic frequencies lower than ω_{PI}, the ion acoustic wave dispersion relationship becomes dispersionless and λ_{IA} is easily calculated as shown in equation (3.3.3).

$$c_s = \lambda_{IA} f_{IA} = \frac{\omega_{IA}}{k} \tag{3.3.3}$$

The plasma will be considered quasi neutral and singly ionized such that the electron plasma density is equivalent to the ion plasma density, or $n_e \cong n_i$. Using an ion plasma density of $n_i = 1e11\ cm^{-3}$ the upper limit to the angular ion acoustic frequency which remains dispersionless is $1.27 MHz$.

For the purposes of this experiment the upper limit of allowable ion acoustic wave frequencies are bounded by the theoretical parameter $\omega_{IA} < \omega_{LH}$. The equation for the lower hybrid angular frequency ω_{LH} is shown in equation (3.3.4). ω_{LH} is a function of ω_{CI} (3.3.5) found in the NRL plasma formulary [18].

$$\omega_{LH} = ((\omega_{CE}\omega_{CI})^{-1} + \omega_{PI}{}^{-2})^{-1/2} \tag{3.3.4}$$

$$\omega_{CI} = \frac{q|\vec{B}_Z|}{m_i} \tag{3.3.5}$$

ω_{LH} is a function of the ion plasma frequency and background magnetic field. Using the plasma parameters chosen for the whistler wave we may excite ion acoustic waves up to $308\ kHz$. This is well below the frequency at which dispersion effects must be considered.

The expected upper limit of electron plasma temperature is $5eV$ for a plasma produced by a steady state RF plasma source where the plasma rests within a chamber with conductive grounded boundaries. Using helium as the ion species and setting a particular excitation frequency, the expected ion acoustic wavelength can be realized.

Using an excitation frequency of $200kHz$ for the above conditions, an ion acoustic wave will travel at a speed of $c_s = 1.1e6\ cm \cdot s^{-1}$ and yield a wavelength of $5.48\ cm$.

The calculated ion acoustic wavelength is on the order of the whistler wavelength (but the velocity is significantly slower) and gives greater confidence that a cylindrical chamber with dimensions of 100cm in axial length and 50cm in diameter should yield an appropriate volume to house the plasma environment and instrumentation.

4 Engineering the Experimental Environment

4.1 Experimental Setup

Figure 4.1.1 illustrates the experimental setup for conducting the parametric antenna experiments.

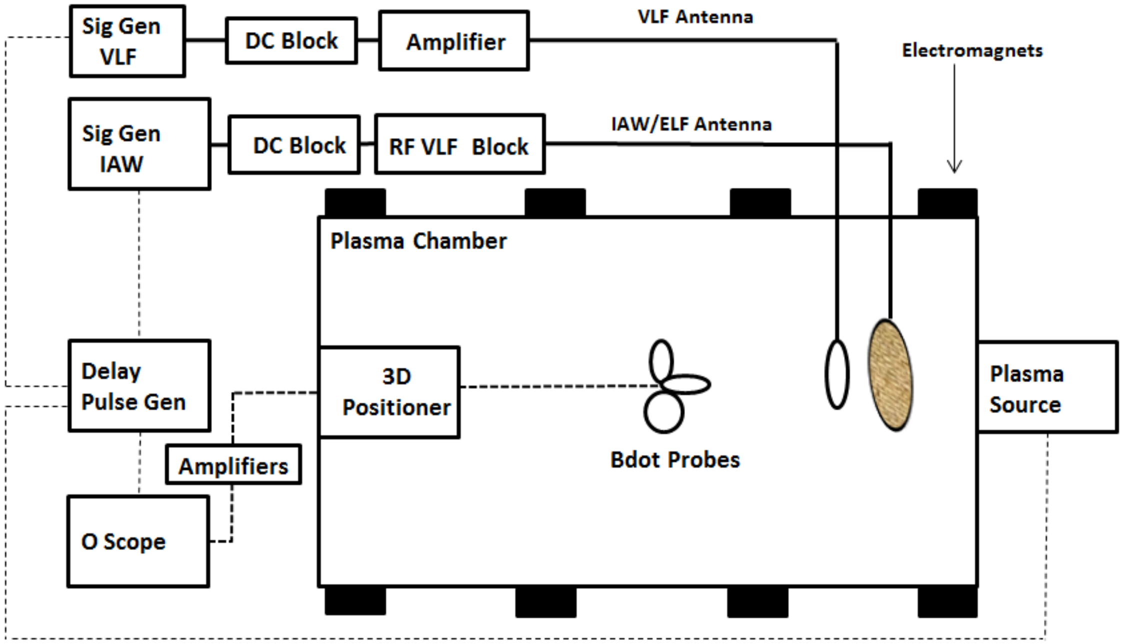

Figure 4.1.1 - *Experimental Setup*

The system as a whole requires several components, some of which will be explained in detail in section 5. A plasma vacuum chamber, electromagnets to generate an ambient magnetic field, a plasma source, signal generators to excite the wave generating antennas, diagnostic devices, positioning stages, and timing equipment to capture plasma parameters and acquire wave data, and finally data processing software.

4.2 Plasma Chamber

A cylindrical stainless steel high vacuum chamber with the dimensions of $100cm$ in length by 50cm in diameter (shown in *figure.3*) was available to be used as a plasma chamber for housing the plasma environment. Several ports ranging in size protruded from the chamber walls. These ports would allow for the introduction of antennas, positioning equipment, diagnostic devices, and a vacuum pumping system.

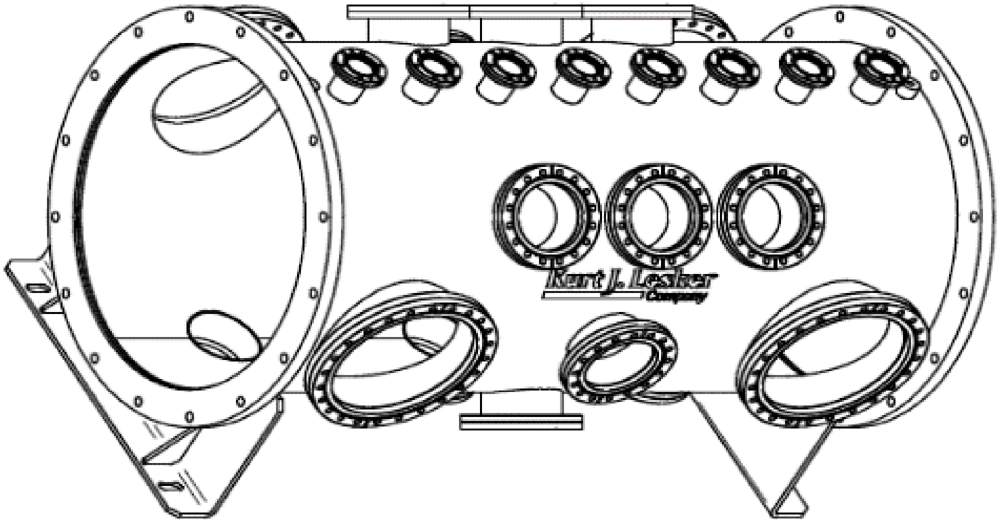

Figure 4.2.1 - *Plasma Chamber*

Gas within the chamber was evacuated by an Edwards B723-01-000 pumping station which consists of a roughing pump and a turbo molecular pump. The chamber is capable of achieving pressures as low as $100\ nTorr$. The pressures are read from a pressure gauge system consisting of two gauges for different pressure regimes.

For pressures at or above $1mTorr$ a convection enchanced pirani gauge is used. For pressures below $1mTorr$ a hot filament ion gauge is used.

4.3 Helicon Plasma Source

A 27.12MHz Helicon plasma source was chosen as the method of plasma generation. These sources remain a cost-effective way to generate plasmas with relatively high densities. The upper limits of reported plasma densities for optimized Helicon sources are on the order of $n_e = 1e13\ cm^{-3}$ as stated by Balkey [17]

Two naturally occurring phenomenon which arises in an RF produced plasma environment must be considered for the experimental study of the parametric antenna. Such phenomenon is the relatively high electron temperature which do not align with cold plasma theory, and the RF noise which will impede the plasma diagnostics. While the plasma source is in steady state operation, electron temperatures will remain relatively high and 27.12MHz RF noise produced by the helicon heating antenna will exist throughout the chamber

To account for these phenomenon, measurements will be made in the plasma afterglow. Immediately after the plasma source is turned off, there is a period of time known as the afterglow which can last on the order of milliseconds. During this period, the electron temperature rapidly decays to sub eV temperatures and most if not all the RF noise from the plasma source will have been absorbed.

Working in the afterglow also presents the challenge of plasma density decay. The electron temperature decays much more rapidly than that of the electron density. By working in a timeframe on the order $10\mu s$ and several microseconds into a plasma afterglow, plasma densities will have decayed by less than an order of magnitude while electron temperatures will have decayed by a full order of magnitude.

Several helicon sources were designed and built. The designs of these sources were based off work done by Francis Chen [19]. The plasma sources were constructed from a $27.12MHz$, $3kW$ power supply, a matching network, quartz glass tube, copper tubing, a water circulator, plastic tubing, and mating components. The permanent magnet source utilized strong neodymium permanent magnet.

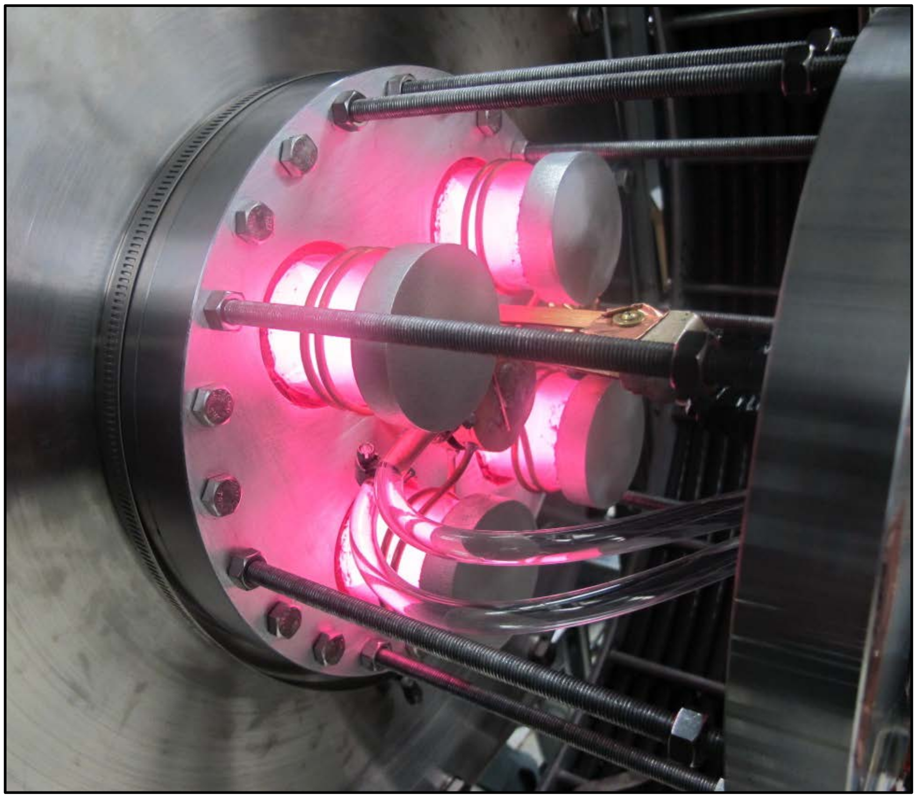

Figure 4.3.1 - *Quad Helicon Source*

A permanent magnet helicon source was the first source built for its ease of construction. A helicon array source was built shortly after to smooth the observed radial plasma density gradients. These measurements will be discussed in the diagnostic section under RF compensated Langmuir probes.

4.4 Electromagnets

With an achievable plasma density in mind, the adjustable parameter of electron cyclotron frequency ω_{CE} will be used to tailor the whistler wavelength. The electron cyclotron frequency is a function of the background magnetic field. By varying the current within large electromagnets placed around the chamber, the electron and ion cyclotron frequencies can be varied.

To achieve the correct value for $\vec{B}_z$ a uniform magnetic field is needed along the axis of the 100cm long chamber. This field will be generated by electromagnets. A simple helmholtz coil configuration consisting of two electromagnets would not be ideal in the facility as the diameter of each electromagnet would need to be at least 2 meters wide, taking up a considerable amount of shared labspace.

By adding additional electromagnets the overall profile of the design becomes more compact as the diameter of these electromagnets will be considerably smaller than that of a basic two coil helmholtz configuration.

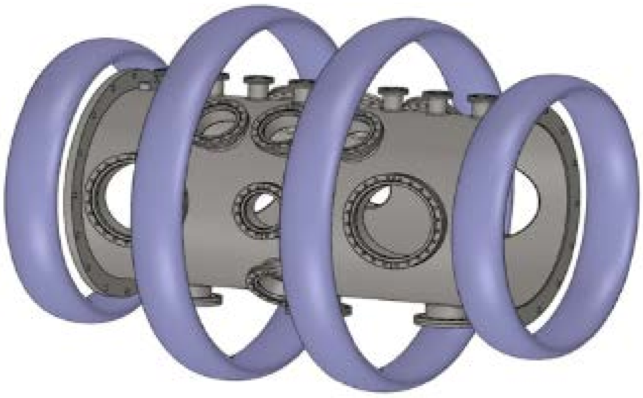

Figure 4.4.1 - *Electromagnet concept*

By simplfying the Biot Savart law to find the axial magnetic field at the center of a current loop shown in equation (4.4.1), and then using the super position of each current loop per electromagnet, a configuration was found which would provide a uniform magnetic field along the axis of the chamber.

$$d\vec{B} = \frac{\mu_0 d\vec{L} \times \hat{r}}{4\pi r^2} \quad \Longrightarrow \quad B_z = \frac{\mu_0 I R}{2(z^2 + R^2)^{3/2}} \tag{4.4.1}$$

An electromagnet constructed from 4/0 shielded copper wire can be relatively inexpensive and low in profile when compared to a water-cooled copper pipe electromagnet. 4/0 copper has a surface area of $107mm^2$ giving a resistance of 1.6e-4 Ohms per meter.

Because resistance is a function of area and temperature shown in equation (4.4.2), the 4/0 copper wire maintains a lower resistance than a hollow copper pipe of the same length and diameter so long as the temperature remains constant.

$$V = IR_{(T,\rho)} \tag{4.4.2}$$

$$R = R_0[1 + \alpha(T - T_0)] \tag{4.4.3}$$

$$R_0 = \rho_{copper} \frac{Length}{Area} \tag{4.4.4}$$

The trade off in value comes at running higher currents. Joule heating will cause the resistance of the 4/0 shielded copper system to increase while a water-cooled copper pipe electromagnet will maintain a constant resistance so long as the temperature is maintained. Furthermore, at higher currents the joule heating can cause the temperature of the 4/0 copper to rise to levels which could degrade the non-conductive jacketing, shorting the electromagnet.

A background magnetic field of approximately $50\ Gauss$ needed to align with parameters of the experiment could be achieved by using only 1 turn of wire per electromagnet, however this would require much more voltage to push the required current. The joule heating shown in equation (4.4.5) of this setup would be unsustainable. By adding more turns of wire, joule heating is minimized.

$$VI = Joule \cdot s^{-1} \qquad (4.4.5)$$

Each electromagnet is a 7x7 row and column of continuous wire for a total of 49 turns per electromagnet. The smaller outer coils have an inner radius of $.38\ m$ and the larger inside coils an inner radius of $.52\ m$. Each coil is separated from one another by a distance of $.38\ m$ The cross sectional area occupied by the jacketed copper wire was considered when evaluating the super position of each turn of wire within each electromagnet. Fields were then calculated.

The current which needs to be applied to the outer coils must be %88.5 of the desired field in gauss and %83.5 for the inner coils. Figure 4.4.2 illustrates the contributing axial magnetic fields from each coil and their summation where 292.5 Amps and 6.44 Volts are applied to the outer coils and 310 Amps and 8.97 Volts are applied to the inner coils. The magnets were ultimately designed to achieve fields higher than $50\ Gauss$ for future experimentation which would require larger ambient magnetic fields.

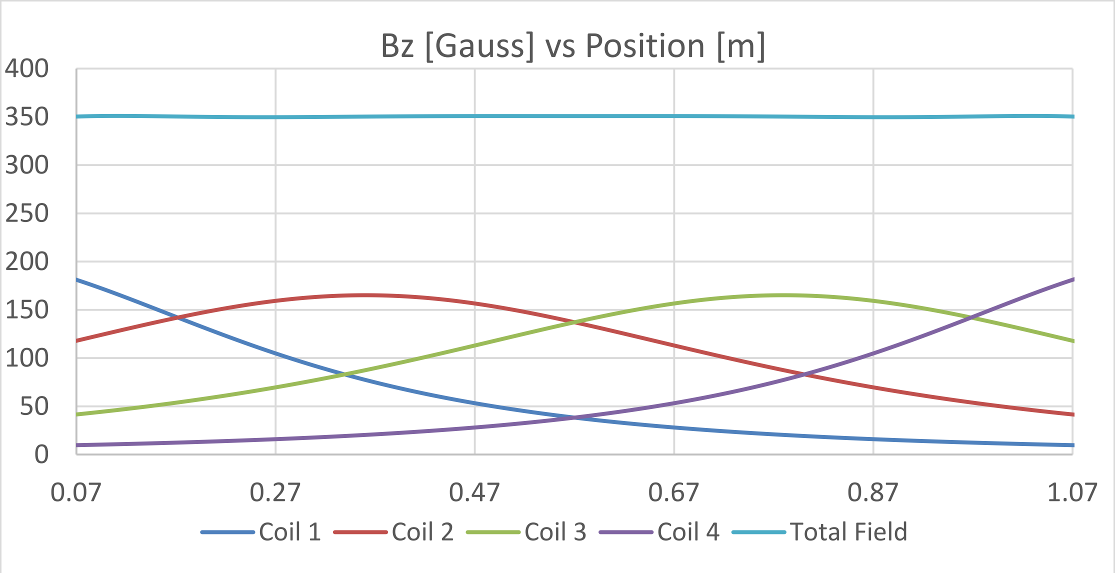

Figure 4.4.2 - *Calculated axial magnetic field* B_z

5 Plasma Diagnostics and Instrumentation

5.1 RF Compensated Langmuir Probe

Langmuir probes are a well-known plasma diagnostic used to determine electron and ion densities, electron and ion temperatures, as well as the plasma potential as shown by Chen [21]. By introducing a conductor into a plasma and applying a potential to the conductor, positive ions and/or negative electrons will be attracted to the conductor and observed as a current.

Several Langmuir probe configurations exist such as single, double, and triple probes. Langmuir probes can be built with RF compensation circuitry as well in the event of their use in steady state RF produced plasmas.

With the use of a single Langmuir probe, one introduces the probe into a plasma and sweeps through a range of potentials and recording the current collected associated with each potential. From this curve described by equation (5.1.1) the saturation region known as the “knee” is shown in Figure 5.1.1. A floating potential (V_f) and a saturation current (I_{es}) are observed as well.

$$I_e = I_{es} \exp\left(\frac{e\left(V_{probe} - V_{es}\right)}{KT_e}\right) \tag{5.1.1}$$

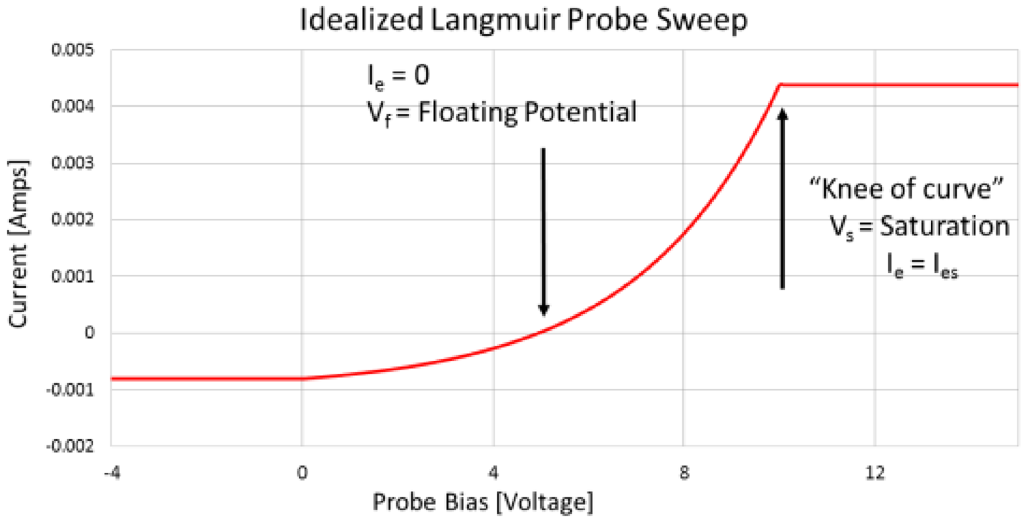

Figure 5.1.1 - *Idealized I-V curve for a single Langmuir probe*

By subtracting off the contributing ion current (there are several methods) and plotting the data from Figure *5.1.1* semi logarithmically, plot Figure 5.1.2 is constructed. From Figure *5.1.2* one can obtain the electron temperature (T_e) from the inverse slope of the region from the floating potential (V_f) to where the saturation region occurs at (V_s).

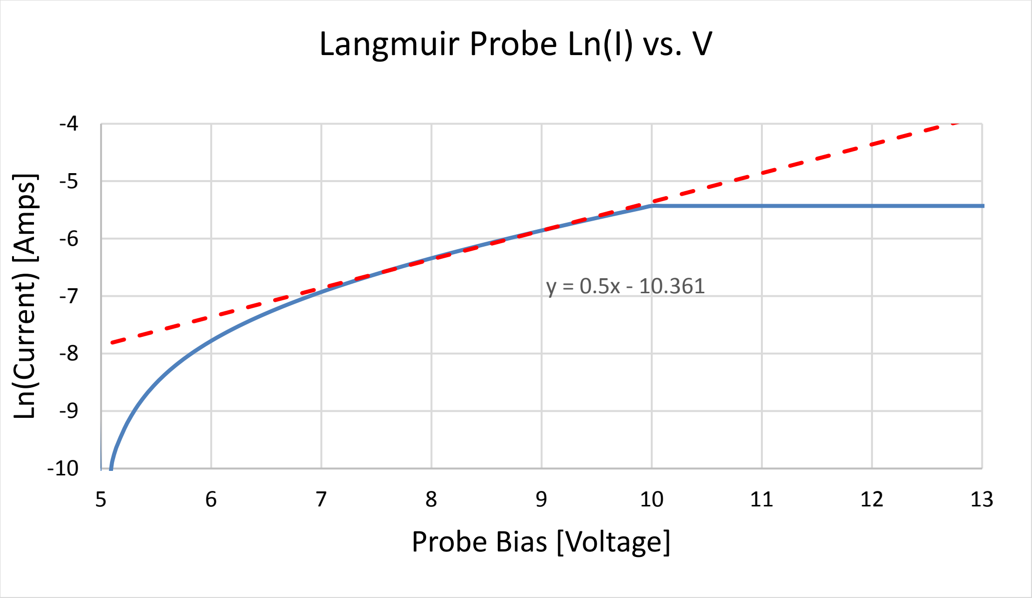

Figure 5.1.2 - *Semi-log plot of an I-V curve*

Plugging in the electron temperature (T_e), the electron saturation current (I_{es}) and the area of the exposed probe tip (A_{probe}) into equation (5.1.2), the electron plasma density can be calculated.

$$I_{es} = en_e \mathrm{A}_{probe}\sqrt{\frac{KT_e}{2\pi m_e}} \Longrightarrow n_e = \frac{I_{es}}{e\mathrm{A}_{probe}\sqrt{\frac{KT_e}{2\pi m_e}}} \tag{5.1.2}$$

Because the plasma source to be used is an RF plasma source, RF compensation circuitry must be added to the Langmuir probe *Figure 5.1.3*. Chen developed the method [22]. RF compensation is accomplished by adding several inductors in series close to the Langmuir probe collection tip as well as introducing a floating electrode coupled to a capacitor. The inductors have a self-resonant frequency of the RF plasma generation frequency (27.12MHz) and the second harmonic (54.24MHz).

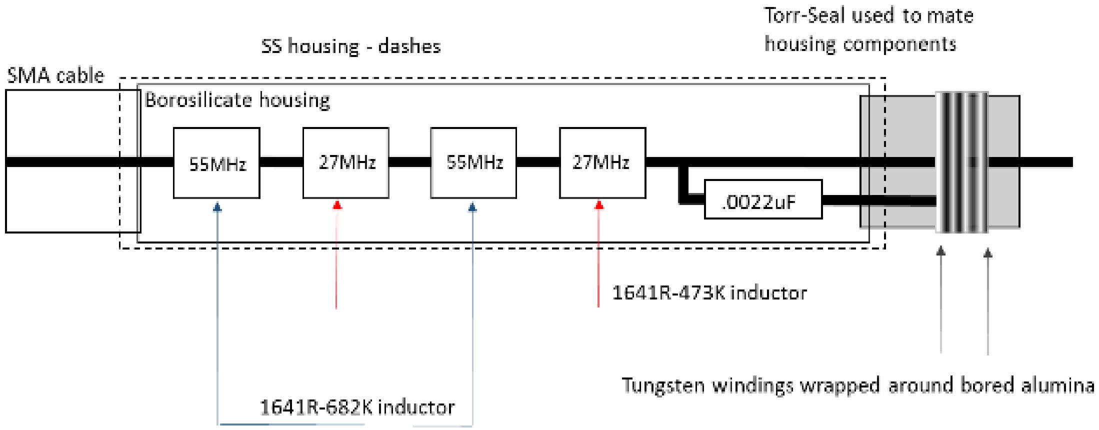

Figure 5.1.3 - *RF compensated Langmuir probe for 27.12MHz plasma source*

The line feeding the sweeping potential to the Langmuir probe is connected to a Keithley 2410 source meter. The Keithley has the capability to output a sweeping voltage while reading a current at the same time. The data of the voltages and currents applied can be extracted through means of communication via computer software. A program called LabVIEW is used to facilitate the remote operation of this device as well as acquire data from the source meter.

The parametric antenna will be tested during the plasma afterglow when the RF plasma source is turned off as to remove the RF noise from the plasma source. For a good estimate of the expected density in the plasma afterglow, ambipolar diffusion as described by Trunec et al [23] in equation (5.1.3) was considered.

$$\frac{\partial n}{\partial t} = -\left(\frac{D_{+p0}}{p_g}\right)\left(1 + \frac{T_e}{T_g}\right)\frac{n_e}{\Lambda^2} \tag{5.1.3}$$

In equation (5.1.3), (D_{+p0}) comprises of the ambipolar diffusion coefficient which has a value of 27 $cm^2 \cdot torr \cdot s^{-1}$ for argon at an initial pressure of 15 $mTorr$. (p_g) is the pressure of the gas while plasma is present which has a value of 16.5 $mTorr$ for 300 Kelvin with respect to the initial pressure at 273 Kelvin. (T_e) is the electron temperature expected to be around 6000 Kelvin for $0.5eV$ in the early afterglow. (T_g) is the temperature of the gas expected to be around 300 Kelvin. (n_e) is the initial electron density set to $1 \times 10^{11} cm^{-3}$ for our expected conditions. Finally, (Λ) is the radius of our plasma chamber which is 25 cm.

Plugging in the above values into equation (5.1.3) yields an approximate density decay of around $5.34 \times 10^6 cm^{-3} \cdot \mu s^{-1}$ in the early afterglow, a 0.005% change in plasma density can be considered constant over the time periods in which wave measurements were performed.

5.2 Bdot Probe

A Bdot probe is a useful diagnostic for acquiring local magnetic field components. A time varying magnetic field will induce a voltage on the probe and this voltage can be read on an oscilloscope. The induced voltage is proportional to the flux of the time varying magnetic field.

An electrostatically shielded Bdot probe Figure 5.2.1 is a diagnostic device used to measure time varying magnetic fields within a plasma. Local charges of the electrons and ions within the plasma can cause electrostatic induction on the probe. Without the shielding, a redistribution of electrcial charges on a naked probe loop would be influenced by nearby charges and be precieved as noise on an oscilliscope.

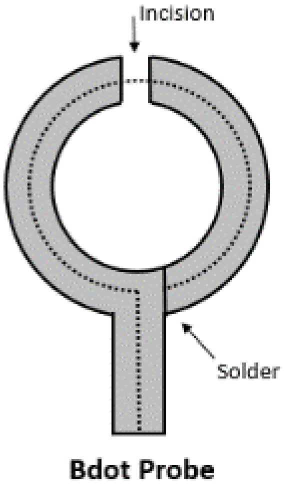

Figure 5.2.1 - *Bdot probe – Electrostatically Shielded Balanced Type*

Utilizing Faraday’s law in equation (5.2.1) we consider the flux through a fixed circular loop shown in equation

(5.2.2) and substitute Biot-Savart’s law to arrive at a magnetic field at the center of the loop as function of current through the loop. Oscillating the current with a fixed frequency (ω) shown in will give a changing flux and meet the conditions needed in equation (5.2.1) to induce a voltage.

(5.2.1)

$$Emf = V = \frac{-N\Delta\phi_B}{\Delta t}$$

$$\phi_B = \oint \vec{B} \cdot d\vec{S} = BA_{probe} \tag{5.2.2}$$

$$V_{(t)} = \frac{-\Delta\phi_{B(t)}}{\Delta t} = \frac{d}{dt}\frac{-A\mu_0 I_0 cos(\omega t)}{2R} = -\dot{B}A_{probe} \tag{5.2.3}$$

$$-\frac{1}{A_{probe}}\int_{t_0}^{t} V_{(t)measured}\, dt = \int_{B_i}^{B_f} dB \tag{5.2.4}$$

$$V_{integrated} * \left(\frac{-A_{probe} * \mu_0 * (I_i - I_f)_{(measured)}}{2R_{Coil}}\right)^{-1} = C_{(f)} \tag{5.2.5}$$

The recorded induced voltage on a probe ideally will give the time varying magnetic field needed to induce said voltage with all other constants known. However, this is not a perfect relation due to inductive and stray capacitive effects and the Bdot probe will have a frequency response. Inductive and stray capacitive effect will cause the voltage reading to be lower than expected; furthermore, the phase difference between induced voltage and the time varying magnetic field can be affected as well.

To derive a true relationship between induced voltage and magnetic field, the Bdot probe will need to be calibrated for each specific frequency to be acquired. The calibration process will give a calibration constants as a function of frequency $C(f)$ shown in equation (5.2.5). These constants can be applied to the integrated voltage reading to ascertain the magnetic field amplitude.

Shielded bdot probes were constructed out of 2.18mm diameter semi-rigid coaxial cable. The end of this cable was bent into a circular loop and then terminated onto itself via solder. Both the center conductor and the outter conducter from the bend head were terminated at the neck of the loop. At the height of the loop above the neck, a small incision was made which disconnects only the outer conductor, forming a gap. The probes were then coated with a ceramic material.

A current loop much larger than the probe loop must be constructed in order to generate a time varying magnetic field with one dimensional component in $\vec{Z}$. A known time varying current with a known frequency is then applied to the current loop and a voltage is read from the loop on an oscilliscope. A signal generator will generate the known frequency while a current monitor (rogowski coil) is used to measure the current applied.

A circular structure was 3D printed to firmly hold a 220mm diameter loop of magnet wire. An Agilent E8257D signal generator was used to generate the time varying current. The current was fed through a 50Ohm SMA transmission line to a Mini-Circuit LZY-22+ signal amplifier. From the amplifier, the line was split as to put the center conductor through a Pearson 6600 current monitor.

The outer and inner conductors were then reattached to an SMA line and fed to the current loop. The center conductor was soldered to magnet wire which was wound around the 3D printed fixture and then connected to the center of a 50 Ohm termination. The outside of the termination was electrically connected to the 50Ohm SMA cable which was fed from the Pearson current monitor. This setup is illustrated in Figure 5.2.2 and the circuit diagram shown in Figure 5.2.3.

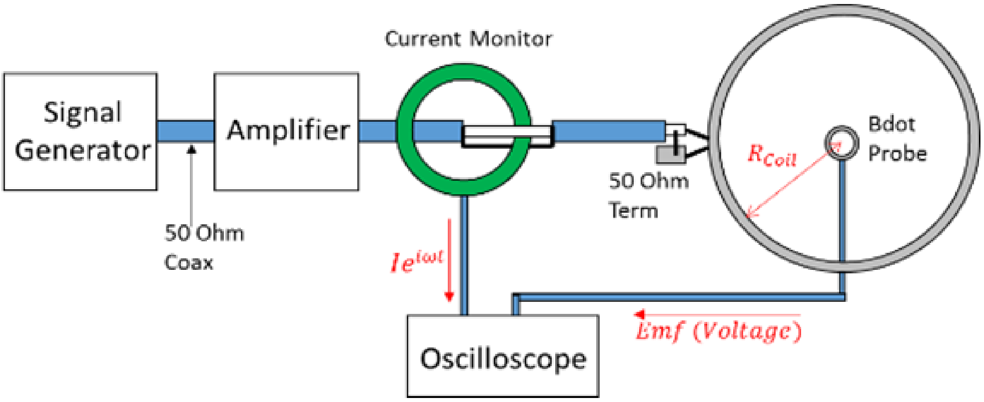

Figure 5.2.2 - *Bdot Calibration Setup*

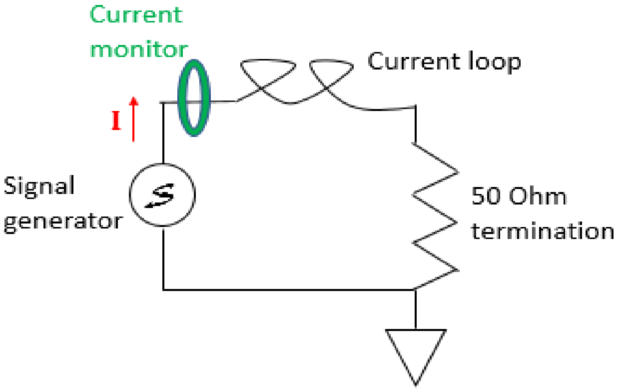

Figure 5.2.3 – *Bdot calibration circuit diagram*

5.3 Positioning System for Diagnostics

A cylindrical positioning system was decided upon as means to mount diagnostics to be used to map out the plasma parameters and the plasma wave topologies to exist within the plasma chamber.

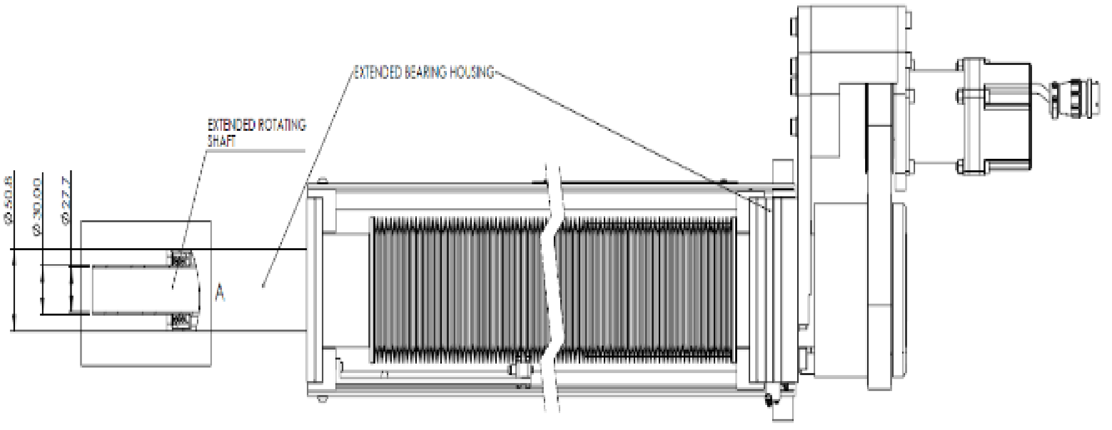

Figure 5.3.1 - *Vacuum Compatible Positioning System*

The ultra-high vacuum positioner Figure 5.3.1 has 800mm of movement along the axis of the chamber noted as the Z direction. The linear resolution per step in this direction is 0.254um. The positioner can also rotate 360^{o} noted as θ. An additional linear stage was mounted to the end of this positioner for diagnostics to be mounted to and give 150mm of movement in the R direction. The combined positioners allow measurements to be taken in a cylindrical coordinate system (Z, R, θ).

Movements of the positioners are controlled by stepper motors which are sent movement instructions through via LabVIEW software. Code was written which allows for automated scans over a defined set of coordinates. Location and amplitude data can then be plotted to give 2D or 3D representations depending on the scan performed.

The center of the positioner has a feedthrough tube to allow coaxial cable and other wires to travel and connect to diagnostic devices. In the case where floating grounds are necessary, hermetically sealed floating ground coaxial feedthroughs Figure 5.3.2 where manufactured in house with the aid of a milling machine and Torr Seal Epoxy.

Manufactures of these feedthroughs offer similar products however the cost of such equipment is considerably more expensive than to engineer in house.

Figure 5.3.2 - *Floating Ground SMA Feedthrough*

5.4 Data Acquisition and Processing

A Tektronix DPO3054 Oscilloscope was used to capture the time varying potentials received on the Bdot probes and the planar Langmuir probe. A Keithley 2410 source meter was used in combination with the RF compensated Langmuir probe to acquire plasma density and temperature measurements. A National Instruments 6212 data acquisition device was used in combination with the AlphaLab GM-2 gaussmeter to acquire the static magnetic data.

The data from these instruments which includes the spatial location of the measurement were stored to files on a computer with the aid of LabVIEW software. This data was then processed and analyzed using Matlab software.

6 Plasma Environment Data

6.1 Magnetic Field

Figure 6.1.1 illustrates a scan of the ambient magnetic field B_z as a function of position. The magnetic field data was acquired from the AlphaLab GM-2 gaussmeter.

This scan was performed over the full 800mm length available to the positioner and covers a circular surface of 100mm in diameter to complete the volume. The field shows to have a variance of roughly 5% throughout the chamber.

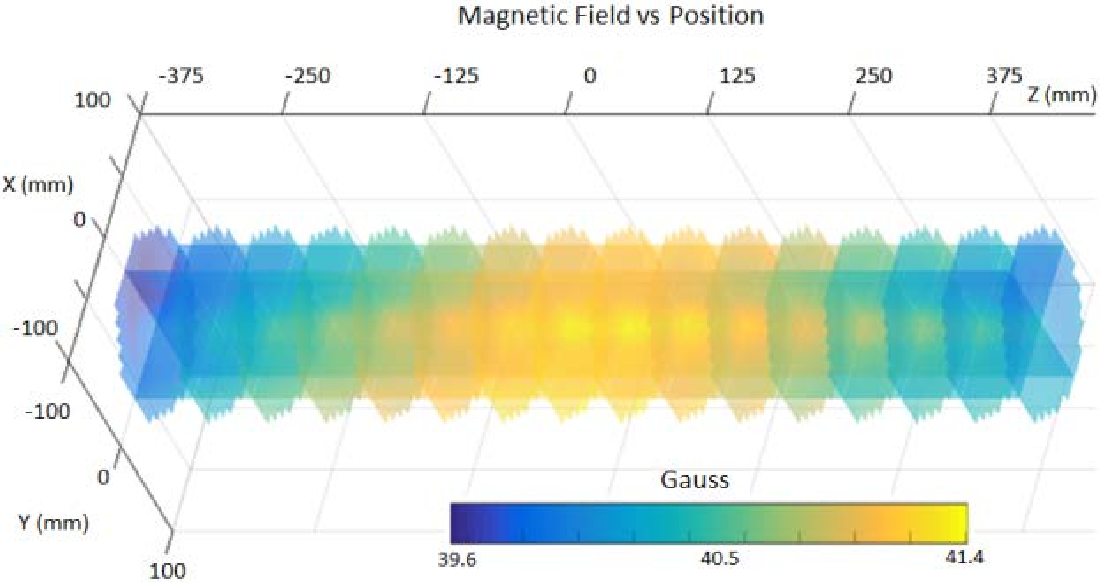

Figure 6.1.1 - *Scan of Ambient Axial Magnetic Field*

6.2 Plasma Density

RF compensated Langmuir probes combined with a 2410 Keithley sourcemeter and LabVIEW software were used to acquire the voltage and current measurements needed to derive the electron plasma density and electron temperatures.

Typical operating parameters for these measurements are as follows; 1.0-2.0kW RF power, 0.1-8 $mTorr$ pressure, 40-60 Gauss. Both argon and helium gas were used.

Plasma densities as high as $6e11\ cm^{-3}$ were realized with the use of Argon at pressures higher than 8 $mTorr$. Helium appeared to yield lower densities than argon when applying the same parameters.

Radial density gradients appeared less pronounced from the quad helicon source than that of the single helicon source. Plasma densities near the helicon plasma source were observed to be higher than towards the back of the chamber. Figure 6.2.1 illustrates the declining density as a function of distance along the chamber axis, away from the plasma source. Figure 6.2.2 displays a radial density scan.

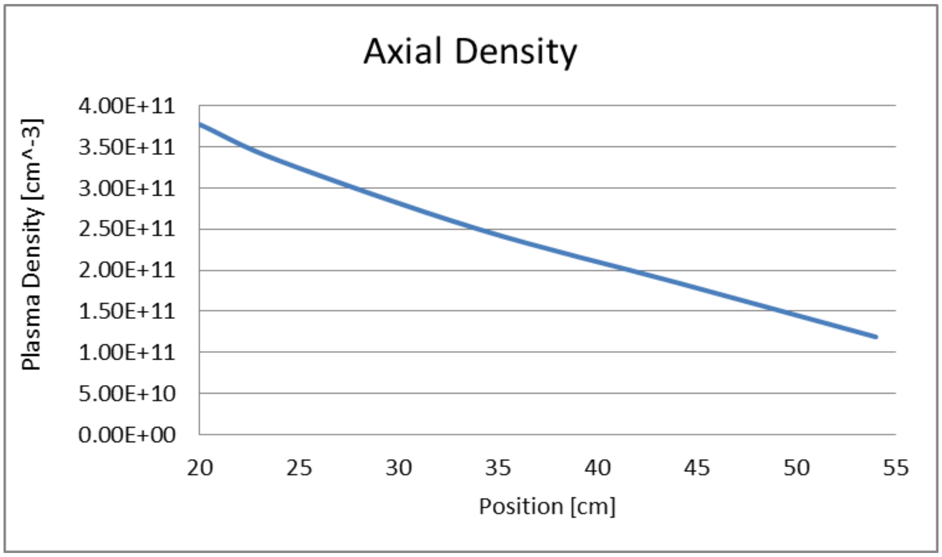

Figure 6.2.1 - *Axial Plasma Density Scan*

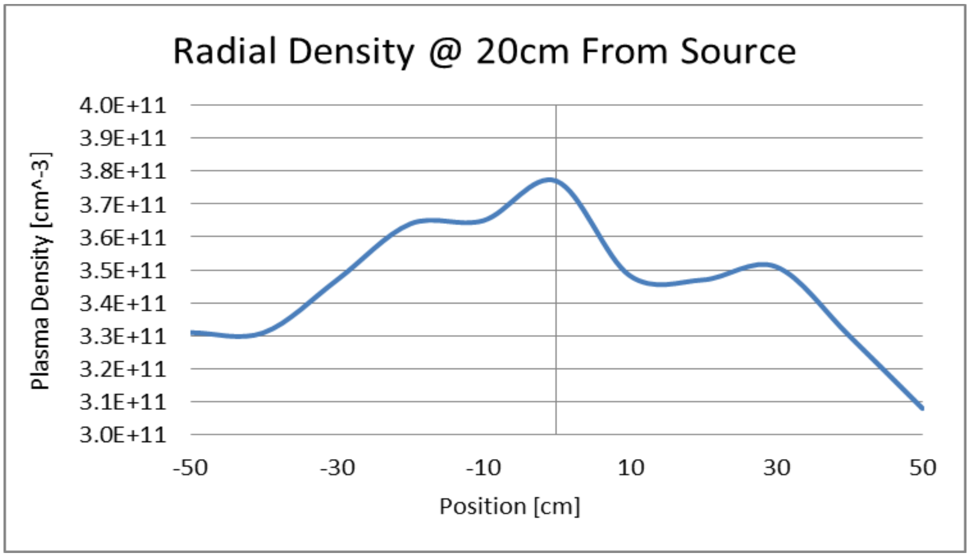

Figure 6.2.2 - *Radial plasma density scan*

Electron temperatures as high as $2.7eV$ were observed with the use of Argon. The temperatures shown in Figure 6.2.3 are derived from the same data as Figure 6.2.1 and shows a declining temperature as a function of distance away from the plasma source

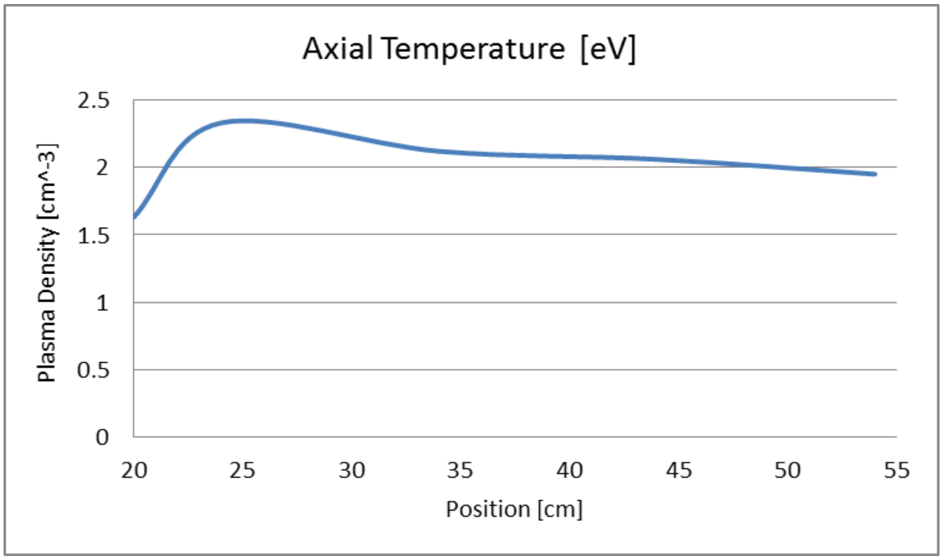

Figure 6.2.3 - *Axial Electron Temperature Scan*

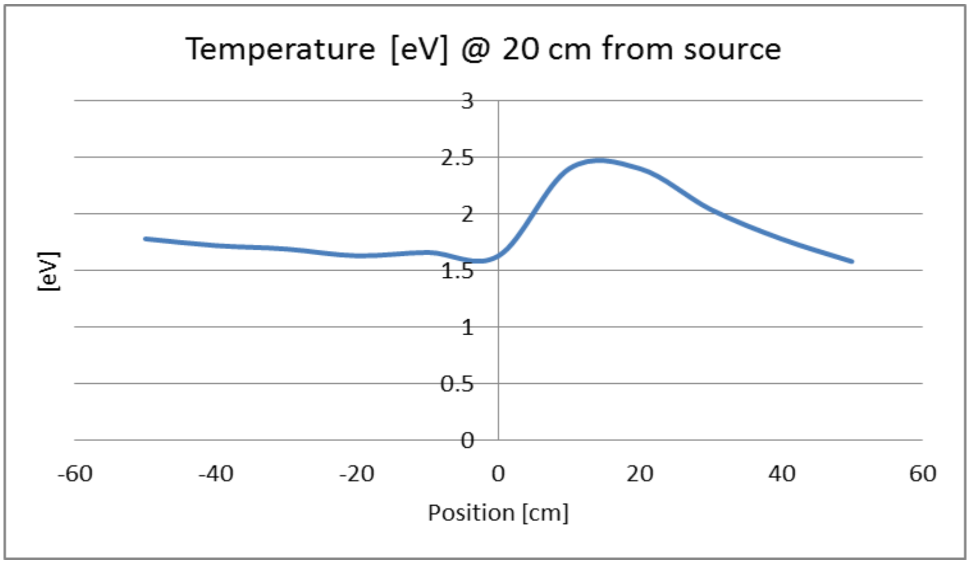

Figure 6.2.4 - *Radial Electron Temperature Scan*

The plasma density decline in the axial direction of the chamber was less pronounced at higher ambient magnetic fields. The same was true for the electron temperatures. Electron temperatures were observed to be higher along the axis of each helicon when using the quad helicon source.

7 Results

7.1 Lower Oblique Resonance

Following similar works to that of Stenzel, Gekelman, Fisher, and Gould, [9] [24] attempts were made to resolve LOR phenomenon with topologies that follow the LOR dispersion relation shown in equation (3.2.1).

A 4cm diameter loop antenna was constructed from semi rigid coaxial cable and magnet wire formed into a loop and soldered onto the inner and outer conductor of the coaxial cable. Unlike Stenzel's works, no balun was available to balance the signal to the loop antenna.

At the time of this experiment, the 3D positioning system was not available. We had access to a simple positioning system which let us scan across a line in the center of the chamber, perpendicular to the chamber axis. The receiving antenna was an exposed center conductor of an insulated semi rigid coaxial cable. The quad helicon array source had not been constructed at this time either and the axial densities decayed from the center of the chamber.

The exciter antenna was excited while the plasma was in steady state at 200 watts of power. The densities were relatively low – between $1e7 - 1e8\ cm^{-3}$. The magnetic field was set to 40 Gauss and the antenna frequency varied between 8MHz and 46MHz while the scan was performed. The receiving antenna was 60mm away from the exciter relative to the center of the chamber.

The power spectrum data from an oscilloscope was saved to a computer and the amplitude of the excitation frequency was plotted as a relative measurement.

The dispersion relation of the LOR predicts a widening of the resonance angle with an increase of the exciter antenna frequency. Figure 7.1.1 appears to show this phenomenon. At 8MHz, the predicted LOR angle is small and the cone tip rests behind the path of the receiving antenna which is located 60mm away from the exciter. At 24MHz the cone tip is located almost directed in the path of the receiver and a narrow spike in the relative RF potential can be seen. At 48MHz the cone tip is well below the receiver and no spike can be seen at the center of the scan.

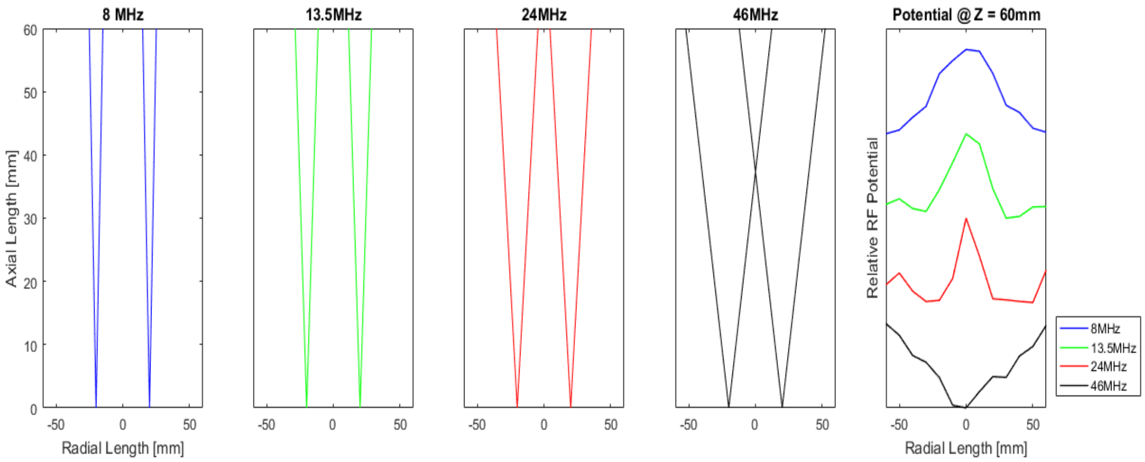

Figure 7.1.1 - *Lower Oblique Resonance Scan*

7.2 Whistler Waves

Whistler waves are generated inside the plasma chamber during the plasma afterglow. It is necessary to perform magnetic field measurements during the plasma afterglow as to avoid capturing RF noise from the helicon plasma source. The helicon plasma source is pulsed on for a length of time order of milliseconds. Then after the plasma source is turned off, the plasma afterglow period begins. 20 μs into the afterglow, the loop antenna is excited and a whistler wave will be launched. The signal generator connected to the loop antenna is triggered from a multi-channel signal delay generator. The signal generator exciting the loop antenna is pulsed for several periods with the same starting phase for each pulse.

Bdot probes connected to an oscilloscope are used to capture the time varying magnetic field which is excited by the loop antenna. The multi-channel signal generator also triggers the oscilloscope. The location at which the time varying signal was captured on the Bdot probe is used as the file name for storing the data for ease of processing. The data is then pieced together to map out the magnetic field topology.

The times of flight measurement technique was applied using Bdot probes to acquire the magnetic field components $Bx_{(x,z)}$, $By_{(x,z)}$, $Bz_{(x,z)}$ in the plane of the y axis. Initial attempts of these measurements involved only a loop antenna and a single Bdot probe. The measurements shown in Figure 7.1.1 illustrate magnetic field topology similar to that of previous experiments of Urrutia [25]. $Bz_{(x,z)}$ & $Bx_{(x,z)}$ shown in Figure 7.2.1 were scanned independently from one another and each show a different wavelength with respect to one another.

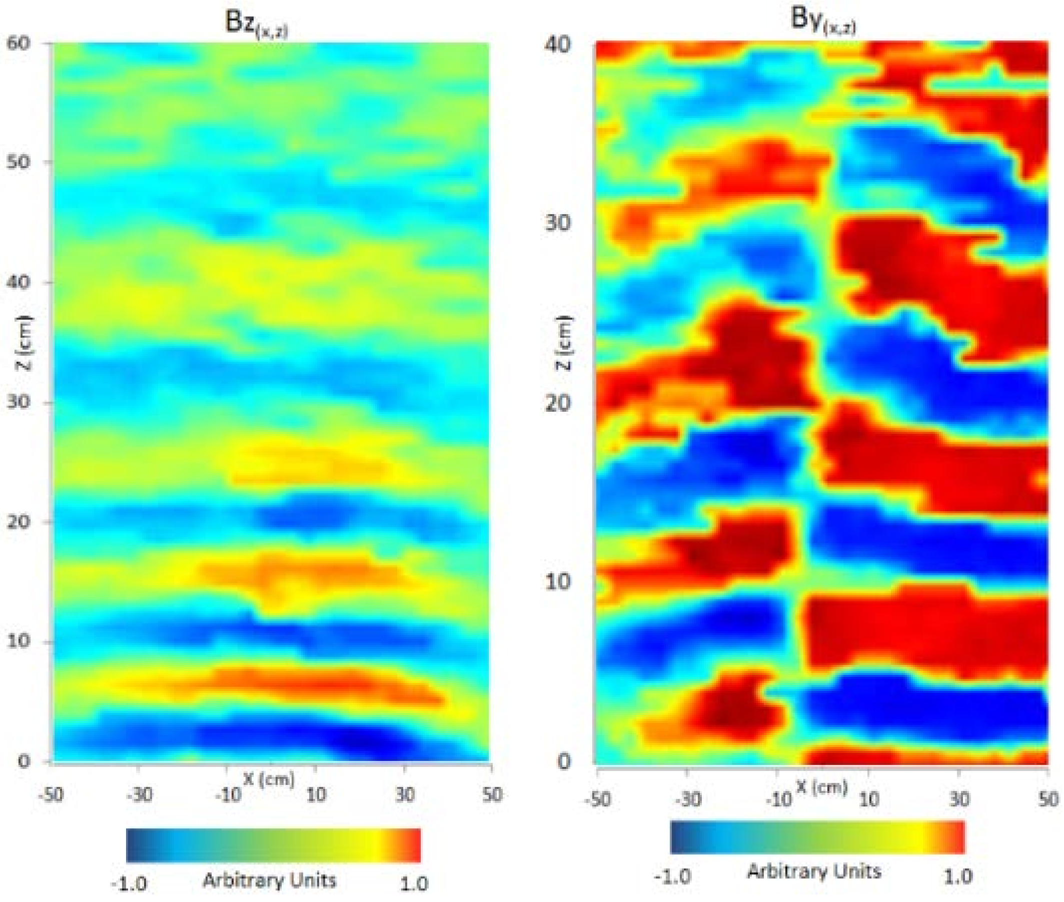

Figure 7.2.1 – *Scan of Whistler Wave Magnetic Field Topology*

The Bdot probes used to make these measurements were approximately 1cm in diameter therefor 1cm was the step size used to position the Bdot probe at each location within the chamber at which a measurement was taken.

For $Bz_{(x,z)}$ in *Figure 7.2.1*, a wavelength of approximately $10cm$ can be observed towards the front of the chamber (position Z = 0cm) and remains constant for approximately $30cm$ into the chamber. This wavelength corresponds to a plasma density of $2e11\ cm^{-3}$ when considering the parameters listed below. The wavelength can be seen shifting into a longer wavelength towards the back of the chamber. This shift in wavelength is likely due to plasma density decay. The parameters below

$Parameters\ for\ Bz_{(x,z)}\ in$ Figure 7.2.1

$f_{Antenna} = 40\ MHz$

$Pressure = 10mTorr\ Argon$

$\vec{B}_z = 40\ Gauss$

$RF\ Power = 1.0\ kW$

A wavelength of approximately $8cm$ can be observed towards the front of the chamber ($Z = 0cm$) in Figure 7.2.1 for $Bx_{(x,z)}$. This corresponds to a plasma density of 3e11cm^{-3} which is slightly higher than that of the $Bz_{(x,z)}$ scan. This is likely due to the increase in RF power as $1.5kW$ was used to generate a plasma for this scan. The wavelength appears to elongate at the location of $30cm$ in the chamber, which is likely a product of density decay.

7.3 Ion Acoustic Waves

A copper mesh screen Figure 7.3.1 with an oscillating potential above the ion cyclotron frequency and below the lower hybrid frequency was used to generate ion acoustic waves. First attempts at generating these waves utilized copper screens with window width spacing of $2\,mm$. This spacing is relative large when compared to the Debye radius of the plasma that was present within the chamber.

Figure 7.3.1 - *Electroformed Copper Mesh - 26 μm Width Spacing*

A planar Langmuir probe with no RF compensation was used to acquire time varying potentials along the axis of the chamber. The probe was negatively biased to $63\ volts$ with 9 volt batteries. The probe was placed $5cm$ from the center of the electroformed copper mesh. At this position, the plasma was pulsed 1000 times while the mesh was excited at $200kHz$ with 1Vpp at $5\mu s$ into the plasma afterglow. Each time varying voltage signal was then averaged and the probe was moved away from the mesh by $5\ cm$ increments with the final position resting $25\ cm$ away from the mesh. The data from the averaged shots are displayed in Figure 7.3.2.

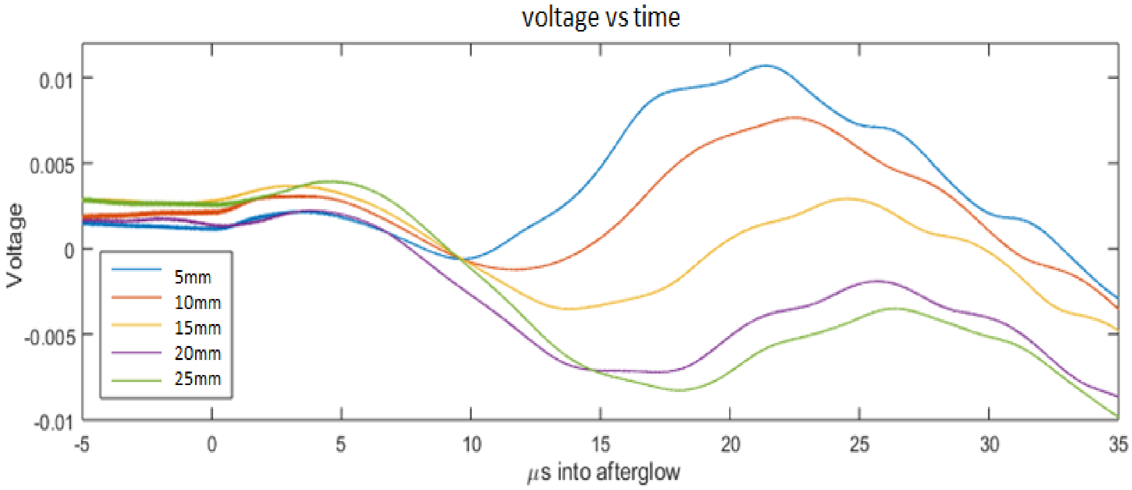

Figure 7.3.2 - *Axial Scan for Ion Acoustic Waves*

A sinusoidal signal can be seen to emerge approximately $10\mu s$ into the afterglow. The signal closest to the mesh at $5\,mm$ shows the largest oscillating amplitudes. These amplitudes show a diminishing trend as the probe is moved further away from the mesh. This is likely due to damping effects from neutral collisions as the ionization percentage of the plasma is less than 1%.

Evaluating the average shift of phase with respect to each position, the ion sound speed velocity was found to be approximately $dx/dt = C_s = 4e5\ cm \cdot s^{-1}$ which is in line with the expected speed of propagation. Helium was chosen as the gas instead of argon for this measurement as faster ion acoustic wave velocities are proportional to lower ion masses.

7.4 Whistler Wave and Ion Acoustic Wave Interaction

The following figures show the setup of the parametric antenna inside the plasma chamber while the plasma source is on. The single helicon source can be seen producing a plasma in *Figure 7.4.1* and the quad helicon in *Figure 7.4.2*. The loop antenna is $60\,mm$ in diameter in both figures and the electroformed copper mesh antenna is approximately $150\ cm$ in diameter.

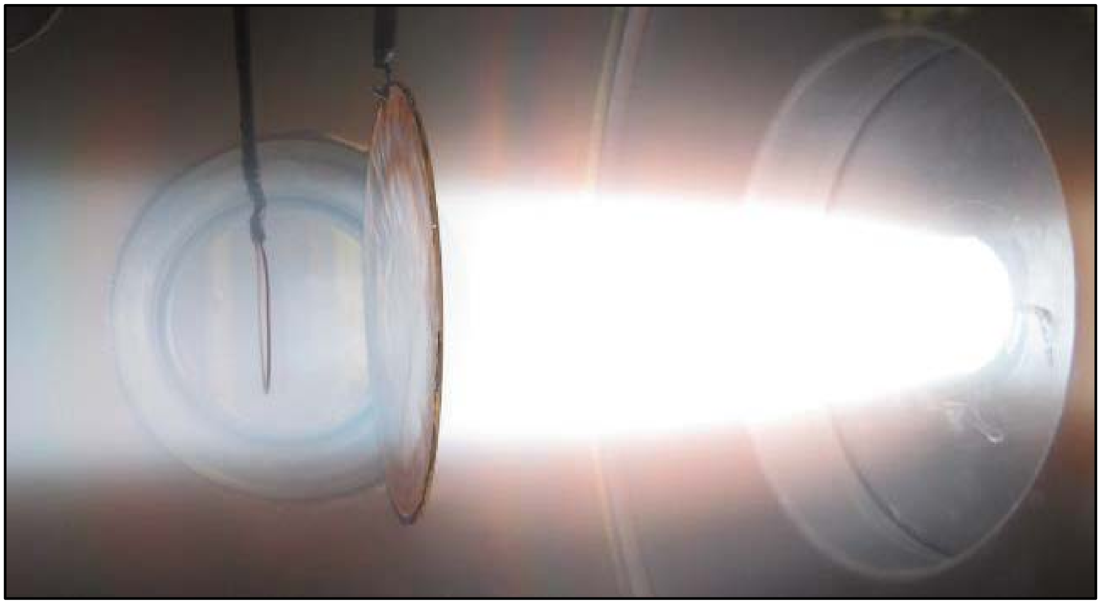

Figure 7.4.1 - *Single Helicon Source*

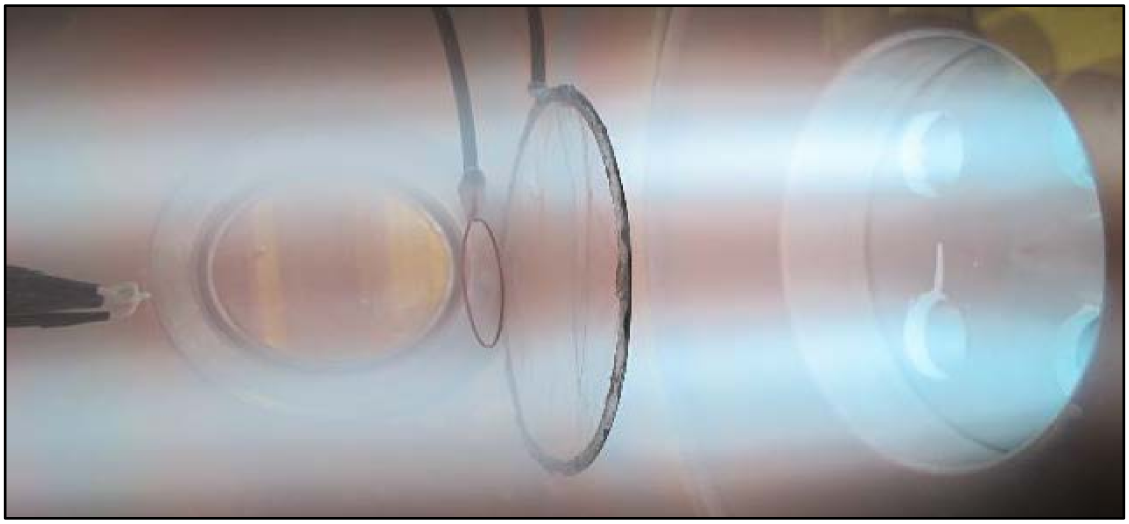

Figure 7.4.2 - *Quad Helicon Source*

Figure 7.4.3 illustrates the magnetic field data acquired from scans performed while a copper mesh was present behind the exciting loop antenna. These scans were performed with three Bdot probes used simultaneously during each pulse and are offset from one another on the X axis by $16\ mm$.

The loop antenna was positioned $25\ cm$ into the chamber from the helicon source. The copper mesh was approximately $8\ cm$ behind the loop antenna towards the helicon source. The Bdot probes used were longer than those used in initial attempts to resolve a whistler wave. The probes extended nearly halfway deep into the chamber due to their additional length, leaving less area for which to perform the measurement. The additional lengths of the overall probes were due to the need of the capability to position the probe at a precise location by bending the semi rigid coaxial cable which they were attached to. The parameters used are listed in *Table 7.1*

Parameters for *Figure 7.4.3*	
n_e	$5 \times 10^{10} cm^{-3}$
T_e	$< 1\ ev$
B_o	$60\ G$
gas	He
$pressure$	$7mTorr$
$RF\ power$	$1.6kWatt$

Table 7.1

Evaluating the topology of the acquired magnetic field, a whistler wave appears to emerge. The topology of this wave is different in appearance than that those which were previous measured in Figure 7.2.1 . A drop in density is the likely cause of this.

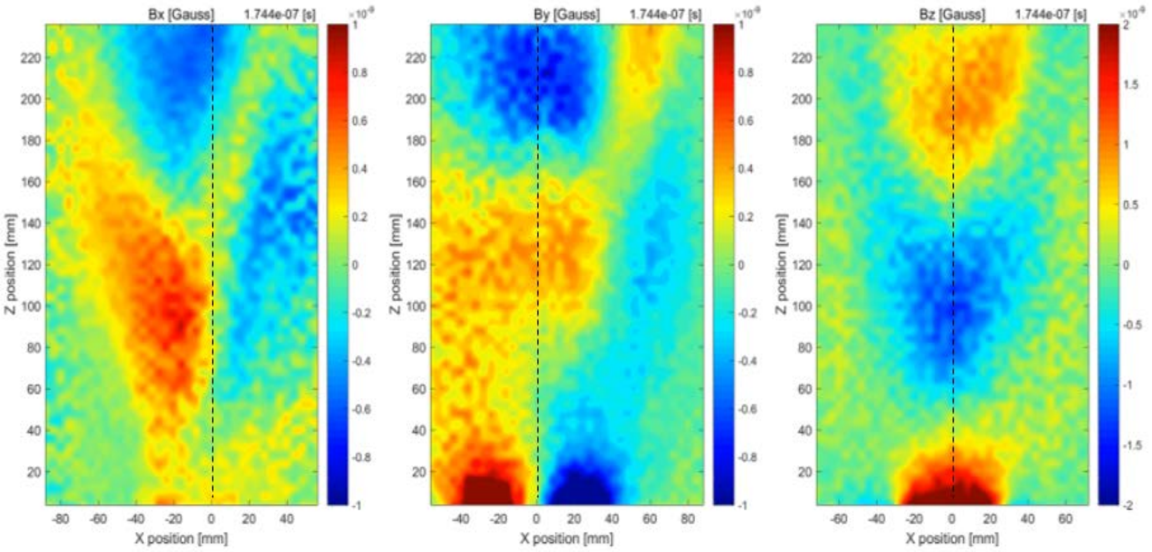

Figure 7.4.3 - *Magnetic Field Topology of Parametric Antenna*

A wavelength of approximately $18\ cm$ was observed from these measurements which correspond to a plasma density of $5e10\ cm^{-3}$. Magnetic field amplitudes were on the order of $10^{-9}\ Gauss$. This density is an order of magnitude lower than what was observed in the initial whistler wave attempts with closely similar parameters. The lower density is likely due to the copper mesh screen absorbing some of the local charges.

Figure 7.4.3 displays the magnetic field components acquired by a Bdot probe while both the loop antenna and the mesh antenna present within the chamber. The parameters for these measurements were the same as Figure 7.4.4

Three different case were attempted; Pulsing only the loop antenna, pulsing only the mesh antenna, and pulsing only the parametric antenna.

The “Loop Antenna Only” and “Mesh Antenna Only” graphs display a smear of a signal over time due to the sample period. Shortening the sample period of the signals shown, the lower graph in Figure, the $40\ MHz$ sinusoidal signals can be seen. Residual $27.12 MHz$ from the helicon source can be seen in the beginning of the signal sample, and is most evident in the “Mesh Only” short sample period graph.

The $200\ kHz$ signal from the mesh antenna is not noticeable in the long sample period “Mesh Antenna Only” graph, as should be expected from an electrostatic wave. The long sample period “Parametric Antenna” graph displays the non-linear behavior and a beating can be seen in the time domain. Towards the end of the long sample of the “Parametric Antenna” graph, the amplitudes of the signal are larger than the amplitudes of the “Loop Antenna Only” as evidenced by the red dotted lines. It is clear that the signals from the

“Loop Antenna Only” and “Mesh Antenna Only” graphs do not add to the signal seen in the “Parametric Antenna” graph.

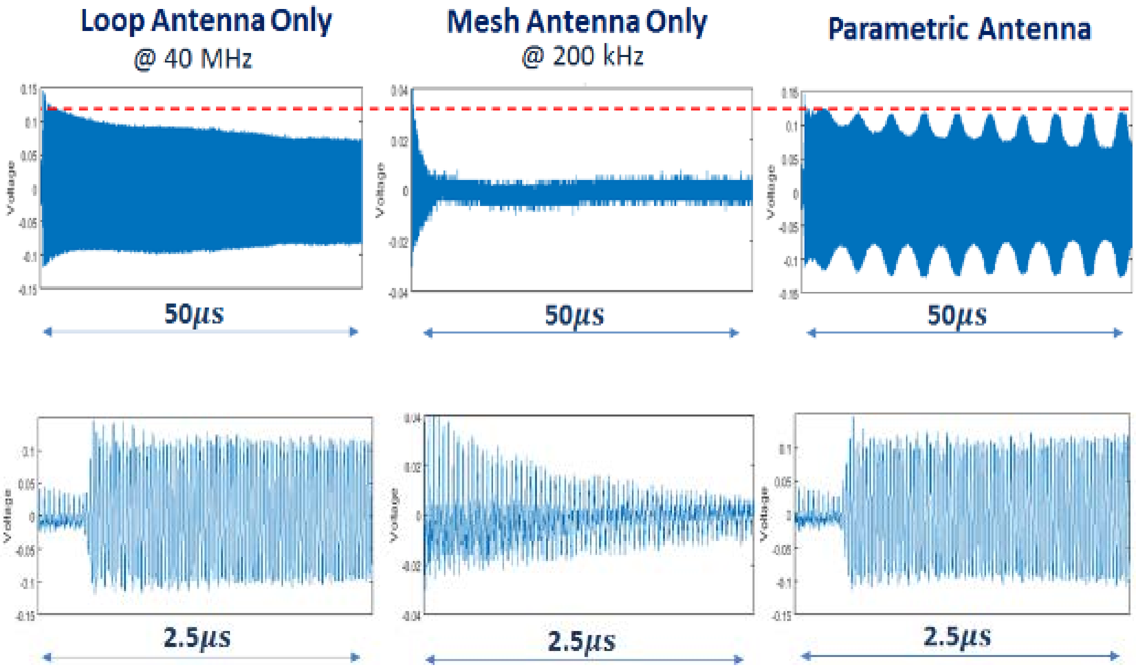

Figure 7.4.4 - *Time Domain Data*

Figure 7.4.5 displays the fast for transform of a signal emitted from the parametric antenna and acquired by a Bdot probe at a particular location within the plasma chamber. The Bdot probe is connected to an amplifier which is then connected to an oscilloscope which can acquire 2.5 Giga-samples per seconds. The time varying signal data from the oscilloscope is imported into Matlab to be processed.

The signal is then truncated to a reasonable length of time which allows the frequency resolution (F_S) to be smaller than that of the ion acoustic frequency by a factor of 10.

This is shown in equation (7.4.1) and subsequent equations while the effects of shortening the sample time (sample points) are illustrated in Figure 7.4.5.

$$F_s = \frac{samples\ per\ seconds}{number\ of\ sample\ points} \tag{7.4.1}$$

$$200kHz = \frac{2.5e9\ samples \cdot s^{-1}}{1.25e4\ sample\ points}$$

$$20kHz^{-1} = 50\mu s\ (sample\ time)$$

The frequency space of Figure 7.4.5 illustrates the three-wave interaction of the whistler and ion acoustic waves. The side band frequencies ($f_w + f_{IA}$) can be seen.

$$f_w = \ whistler\ frequency = 40MHz$$

$$f_{IA} = \ ion\ acoustic\ frquency = 200kHz$$

$$f_w + (c)f_{IA} \ = \ 40MHz \pm (c)200kHz\ , \qquad c = 1{,}2{,}3\ ...$$

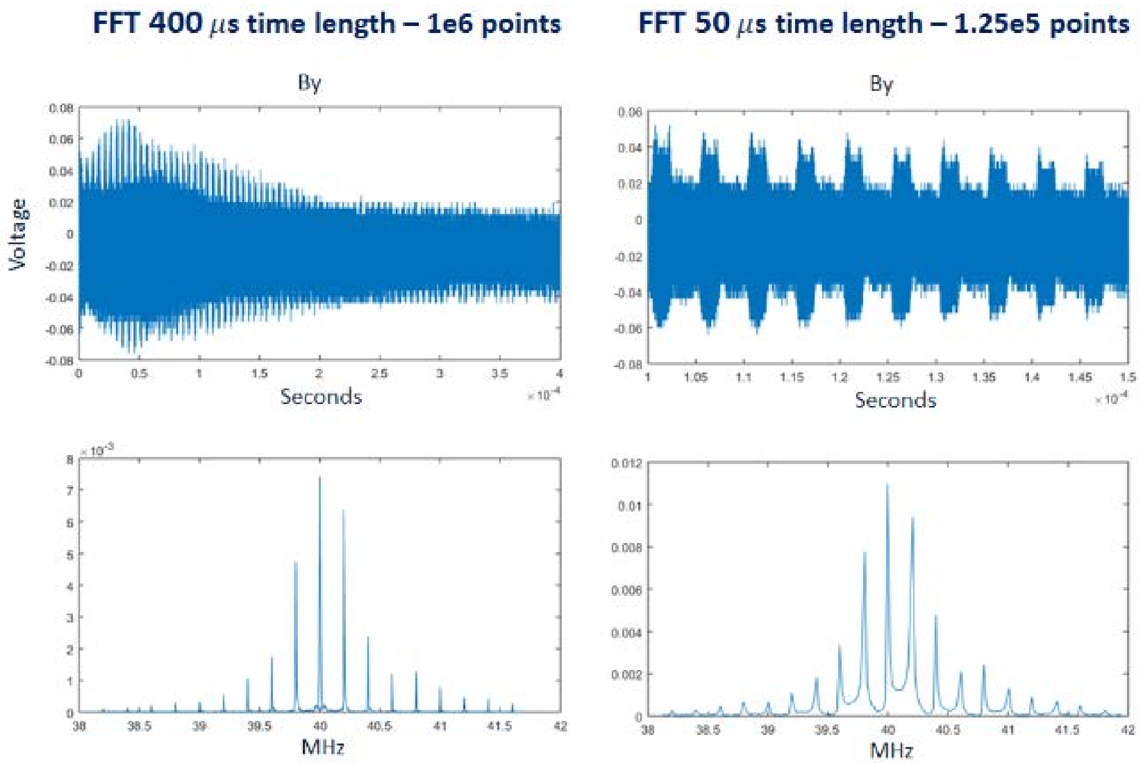

Figure 7.4.5 - *FFT of Same Signal at Different Sample Times*

The parameters listed below parameters were used for examining different conditions at a location were parametric activity was noticeable. The different conditions were; with and without the excited copper mesh, varying the power into the loop antenna, varying the time at which the FFT was performed.

$$Parameters$$

$$f_{Antenna} = 60\ MHz \qquad \vec{B}_z = 60\ Gauss$$

$$RF\ Power = 1.5\ kW$$

$$Ion\ Acoustic\ Antenna = 10Vpp\ @\ 200kHZ$$

$$Center\ of\ Loop\ Antenna\ Location = (x, z) = (0mm, 0mm)$$

$$B_x\ \ Bdot\ location = (x, z) = (50mm, 50mm)$$

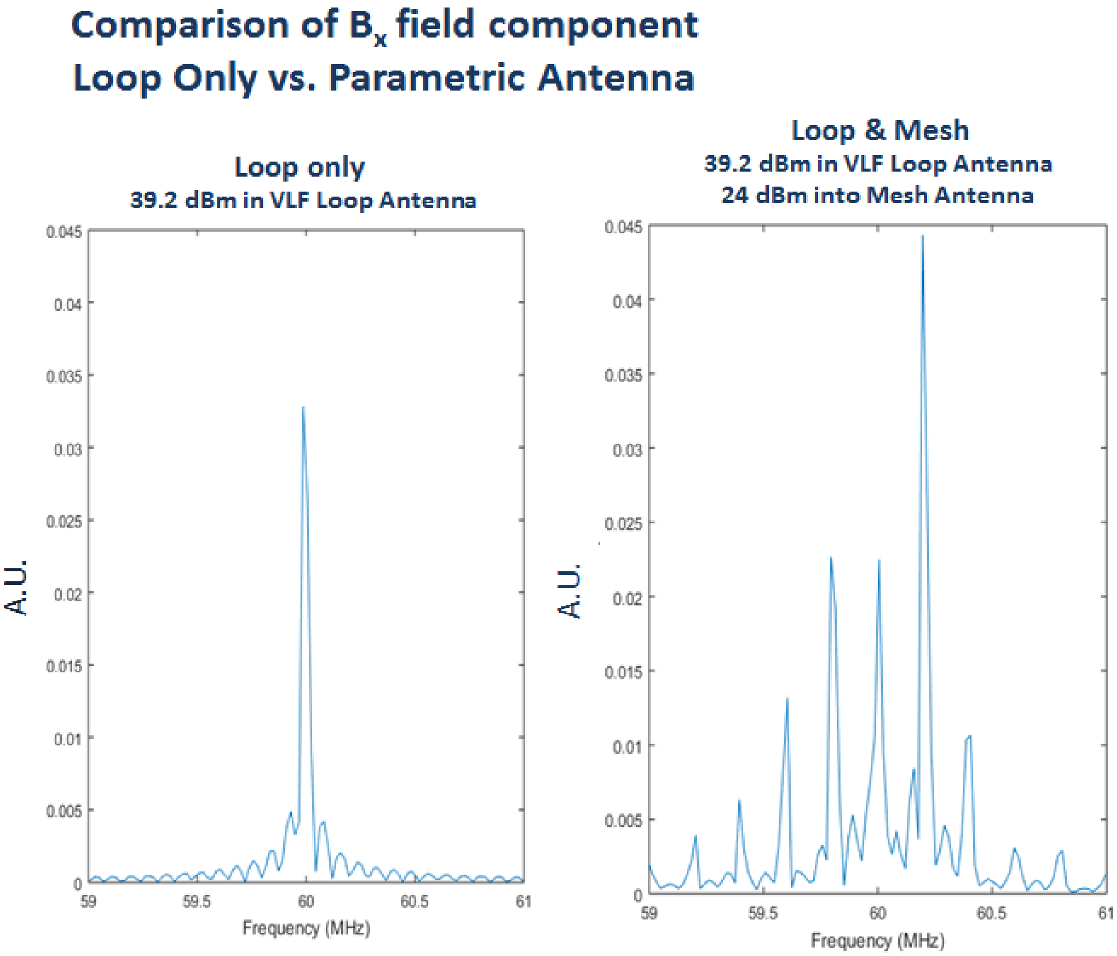

Figure 7.4.6 - *FFT, with and without Excited Mesh*

Figure 7.4.6 displays two different cases of an FFT performed on signal taken at approximated 130 μs into the plasma afterglow. Pressure of the system was held at 7 $mTorr$ of Helium. No sidebands are present in the case with only the loop antenna excited. Several sidebands are apparent with the addition of the excited mesh antenna. The sidebands are at integer distances in frequency of 200 kHz from the center frequency.

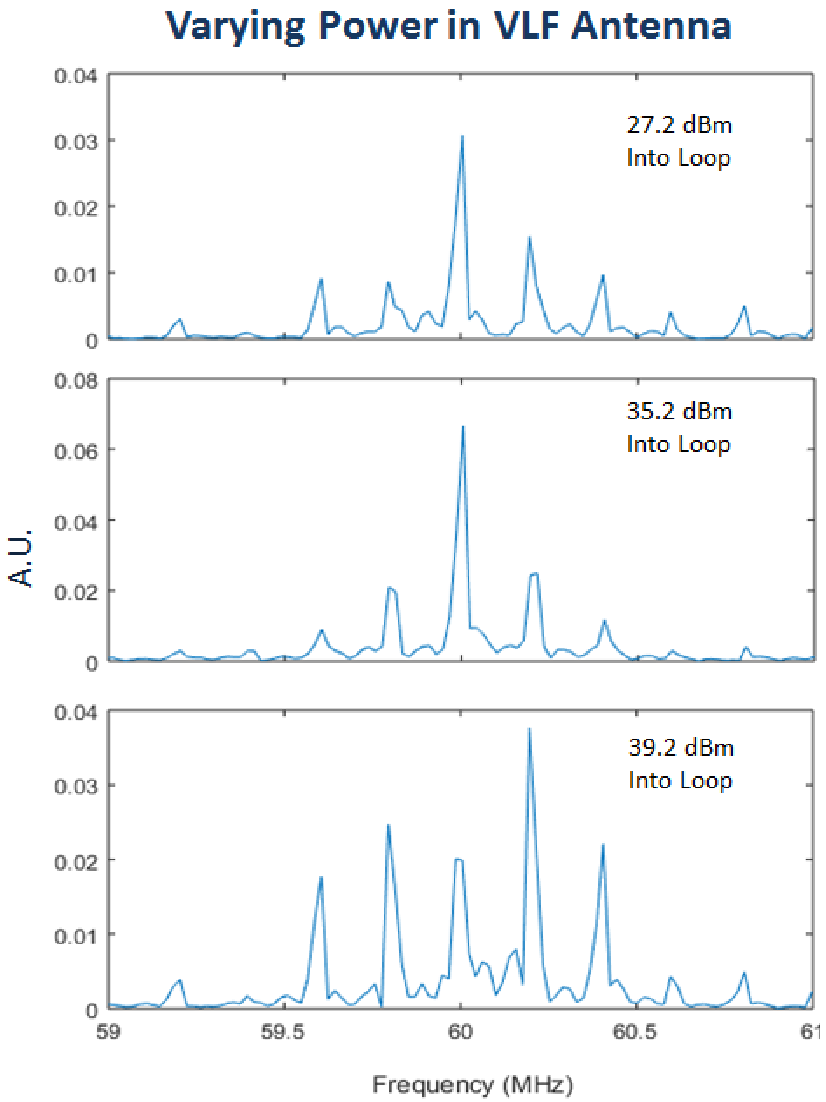

Figure 7.4.7 - *FFT Varying Power*

The power into the loop antenna shown in Figure 7.4.7 was varied and recorded at three different power levels. The time the FFT was performed begins at 130 μs into the afterglow and for a length of 40 μs. Pressure of the system was held at 7 $mTorr$ of Helium. Sideband frequencies showed higher amplitudes relative to the center band frequency at the highest setting 39.2dBm.

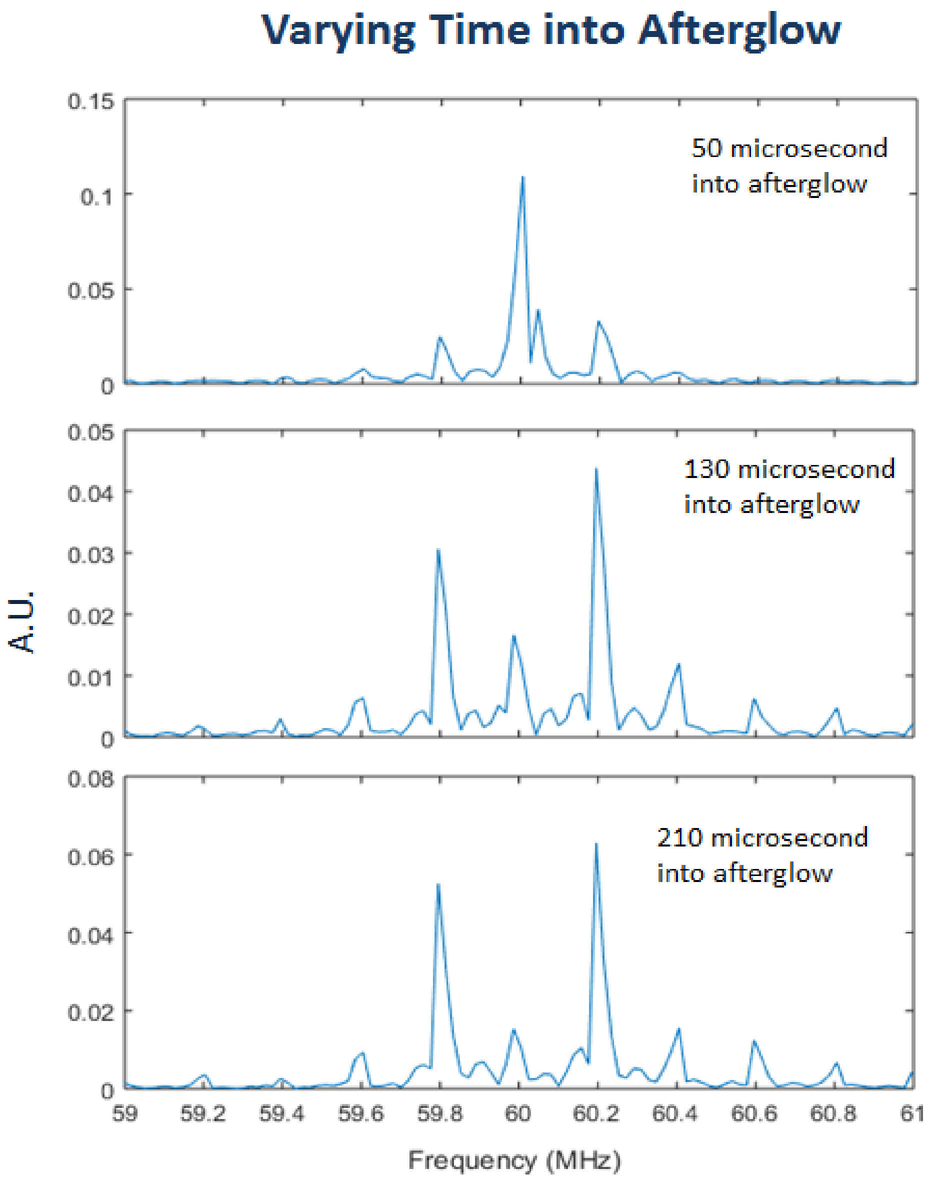

Figure 7.4.8 - *Varying Time into Plasma Afterglow*

With the power into the loop antenna held at $35.2\ dBm$, sideband amplitudes were evaluated at different times withing the afterglow. The length of time the FFT was performed over was $30\ \mu s$ and the segment of time which the FFT when performed was varied and recorded at three different times. Pressure of the system was held at $3.2\ mTorr$ of Helium. Sideband frequencies showed higher amplitudes relative to the center band frequency later into the afterglow. Electon temperatures later into the afterglow are expected to have relaxed.

The time varying data taken at each point in a plane for each component $Bx_{(x,z)}$, $By_{(x,z)}$, $Bz_{(x,z)}$ had a recorded length of $400\ ms$. The spacing of dx and dz within the plane was $4mm$, which is the diameter of each Bdot probe.

The plane of measurement spanned a distance of $230\ mm$ away from the loop antenna noted as the Z axis and $\pm 70\ mm$ to the left and right of the center of the loop antenna noted as X axis. From each spatial location, a fast Fourier transform was applied over a length of time $30\ \mu s$ from the beginning of the time varying data. Later into the time varying data this transform was performed again. The frequency components were then separated and plotted in their respective locations. The center frequency of $60\ MHz$ was plotted on one graph while the summation of the sideband frequencies $60\ MHz\ \pm C * 200\ kHz, C = 1{,}2$ was plotted on another graph. This concept is illustrated in Figure 7.4.9 and the data is shown in Figure 7.4.10***Error! Reference source not found.*** and Figure 7.4.11. - The data was acquired using the same parameters listed in Table 7.1

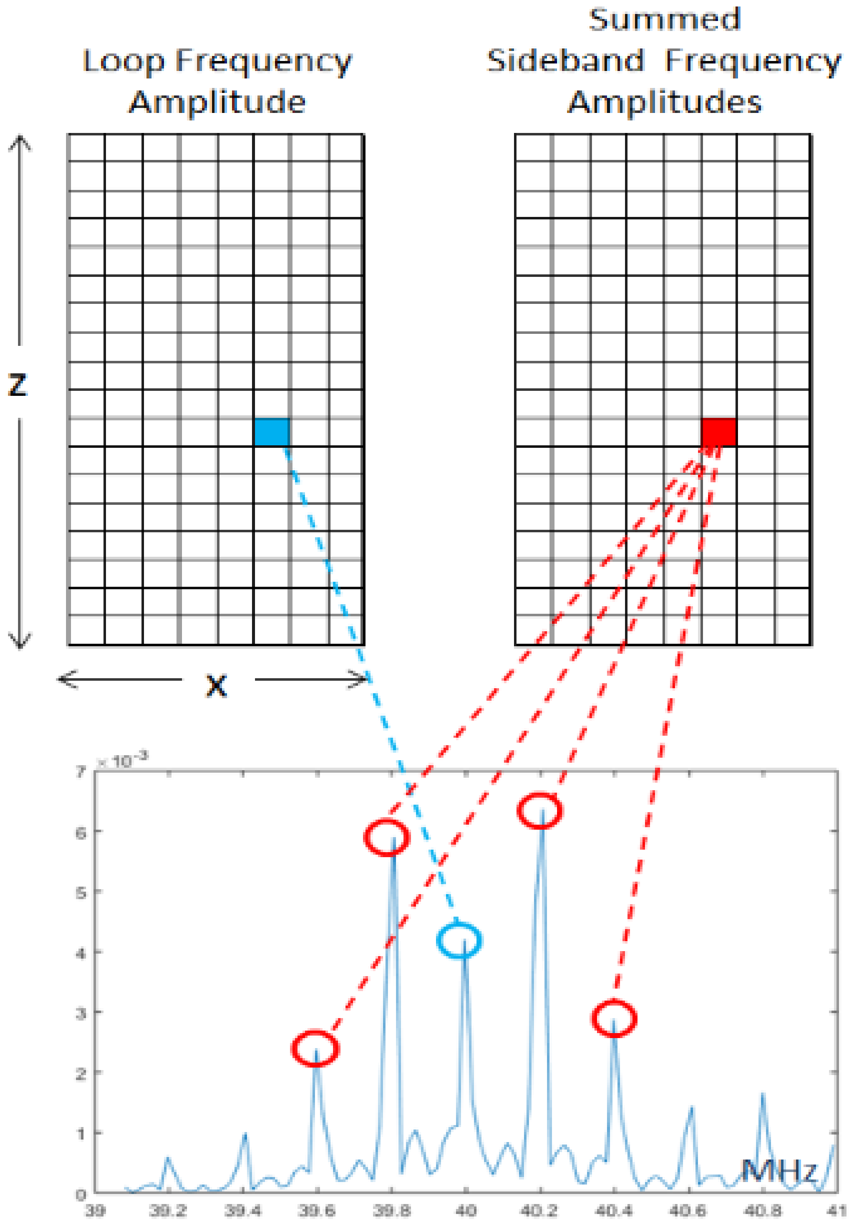

Figure 7.4.9 – *Plotting Frequency Coefficients*

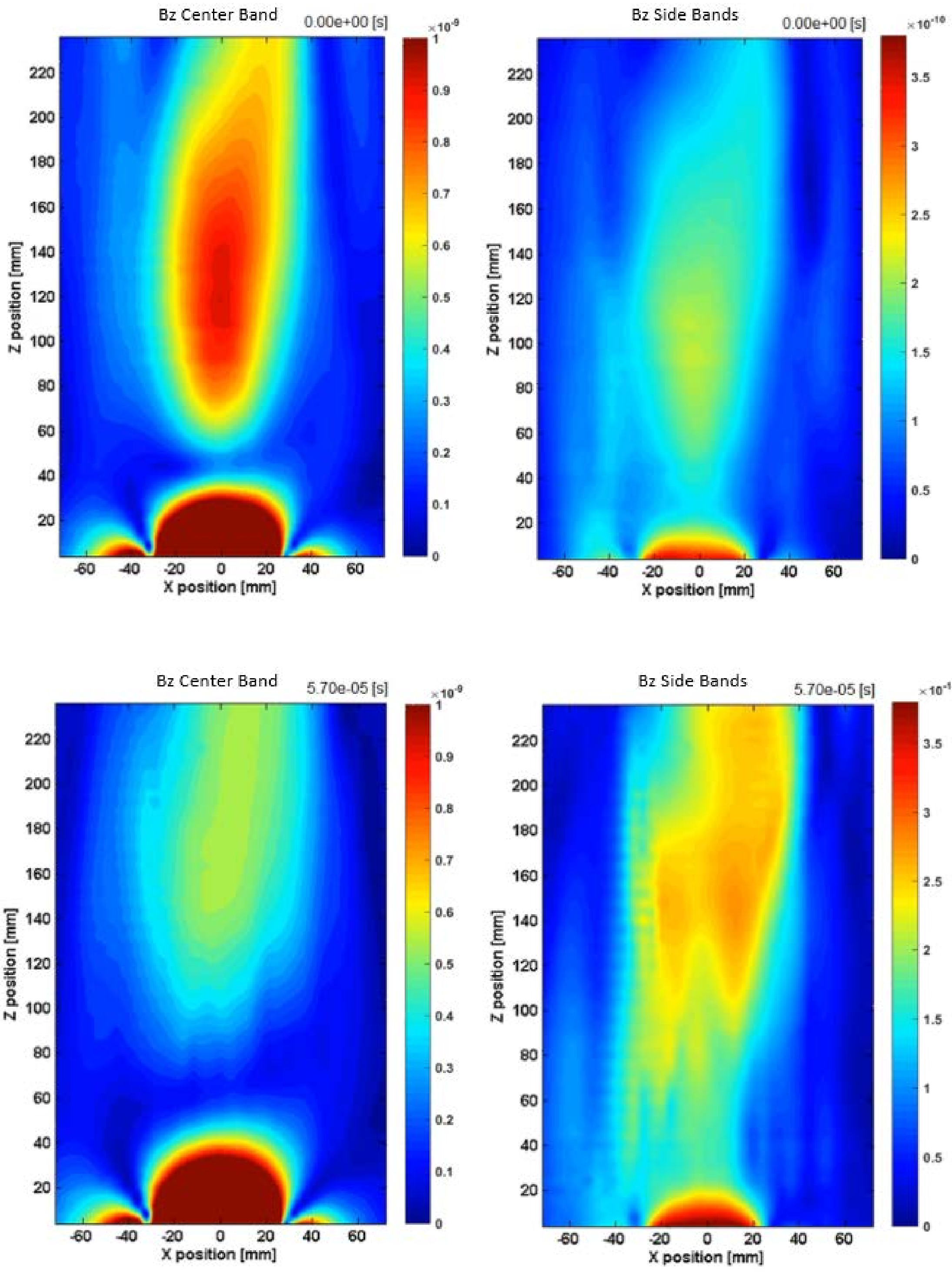

Figure 7.4.10 - $Bz_{(x,z)}$

Top Picture - Immediate Afterglow, Center Band and Summed Sidebands

Bottom Picture - 110 μs *into afterglow, Center and Summed Sidebands*

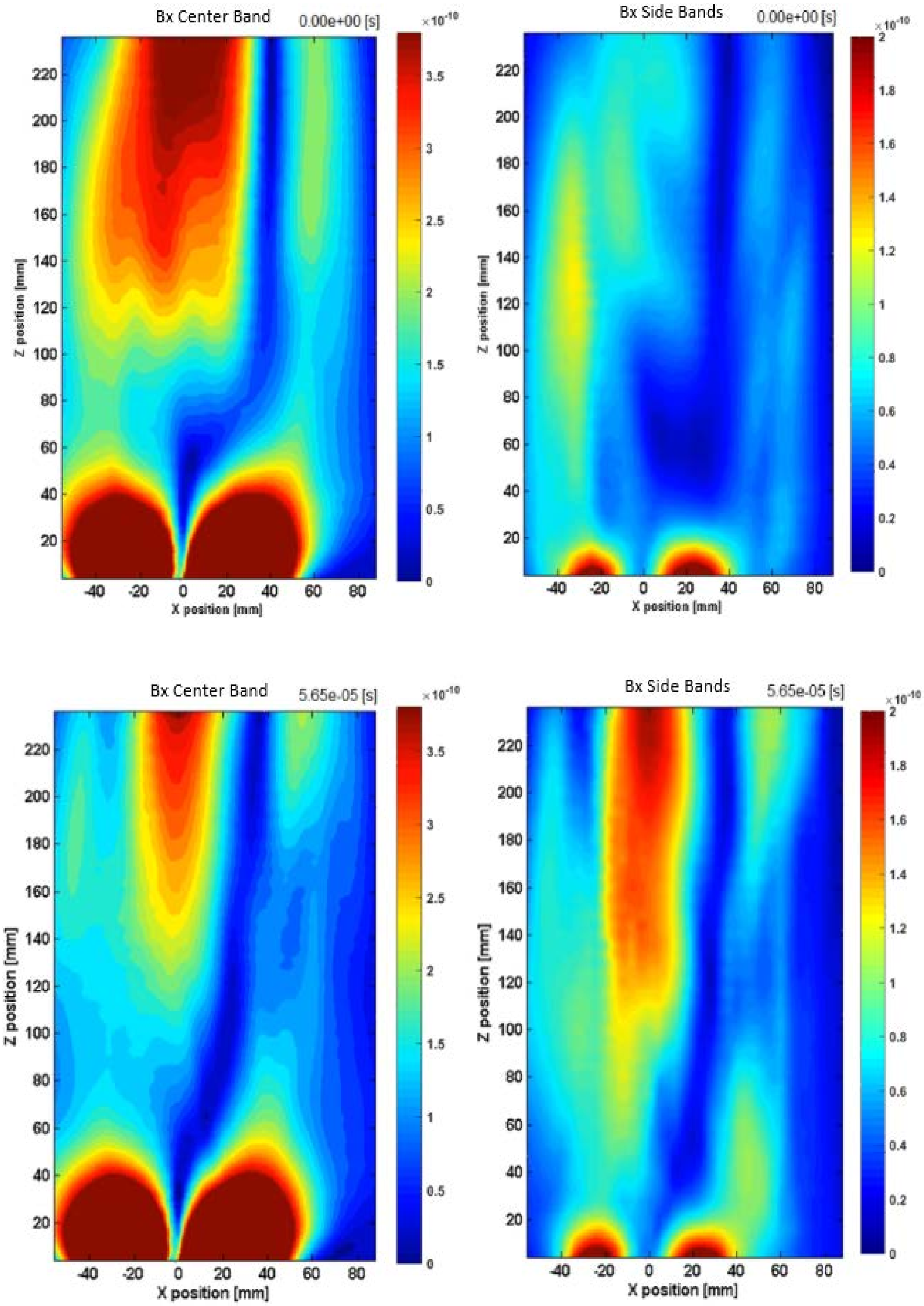

Figure 7.4.11 – $Bx_{(x,z)}$

Top Picture - Immediate Afterglow, Center Band and Summed Sidebands

Bottom Picture - 110 μs *into afterglow, Center and Summed Sidebands*

The top left graph in Figure 7.4.10 displays the amplitudes of $Bz_{(x,z)}$ of the center band frequency $60MHz$ extracted by a fast Fourier transform FFT. The FFT takes place immediately into the plasma afterglow at the beginning of when the loop antenna is excited. The top right graph in the same figure displays the summation of the side band frequencies with the same amplitude extraction method applied. Comparing the top left and right graphs in , the summation of the sideband frequencies are relatively smaller compared than the center band.

The same methods were applied to the lower left and right graphs in with the FFT applied $110\ \mu s$ after the loop antenna was excited in the plasma afterglow. The summed sideband frequencies can be seen to have relatively similar amplitudes to that of the center frequency.

Figure 7.4.11 illustrates the same methods that were applied in. The $Bx_{(x,z)}$ frequency components are evaluated at two different times when the loop is excited in the plasma afterglow. The top two graphs evaluate the components immediately after the loop antenna is excited. The bottom two graphs evaluate the components $90\ \mu s$ after the start of the loop antenna excitation.

The summed sideband frequency amplitudes of one of the particular components $Bx_{(x,z)}$, $By_{(x,z)}$, $Bz_{(x,z)}$ at a particular location and time are divided by the center frequency amplitudes of the same component at the same location and time to produce a ratio. These ratios are then plotted in their respective location in the plane of measurement to convey where the sideband frequencies are more or less pronounced in comparison to the center frequencies. This concept is illustrated in Figure 7.4.12 and data is shown Figure 7.4.13. The data acquired from Figure 7.4.13 was done using the same parameters as listed in Table 7.1

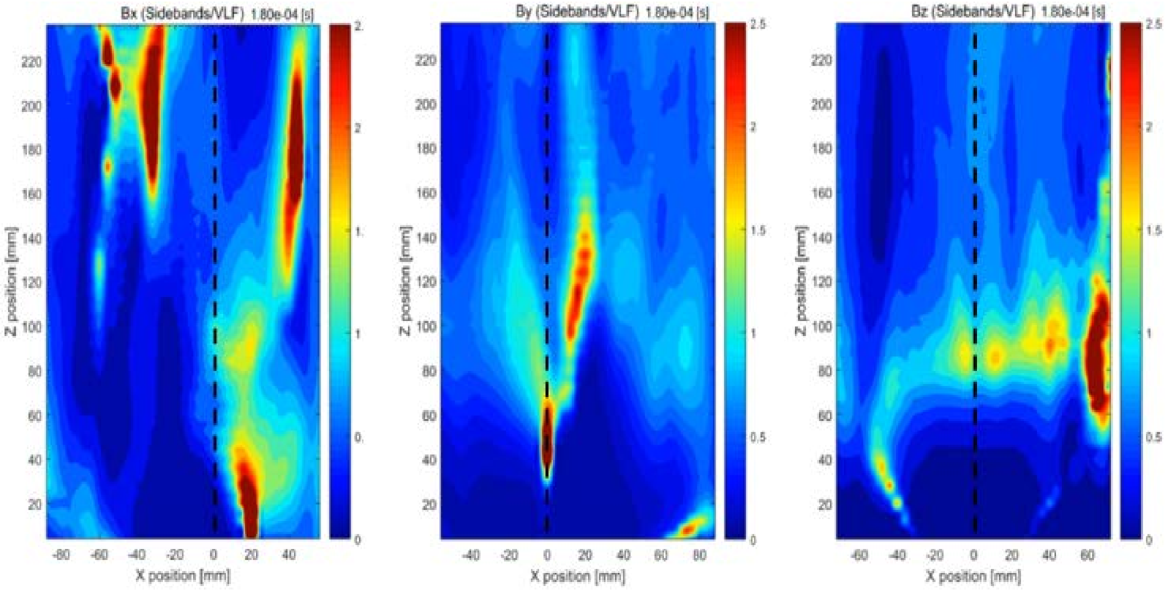

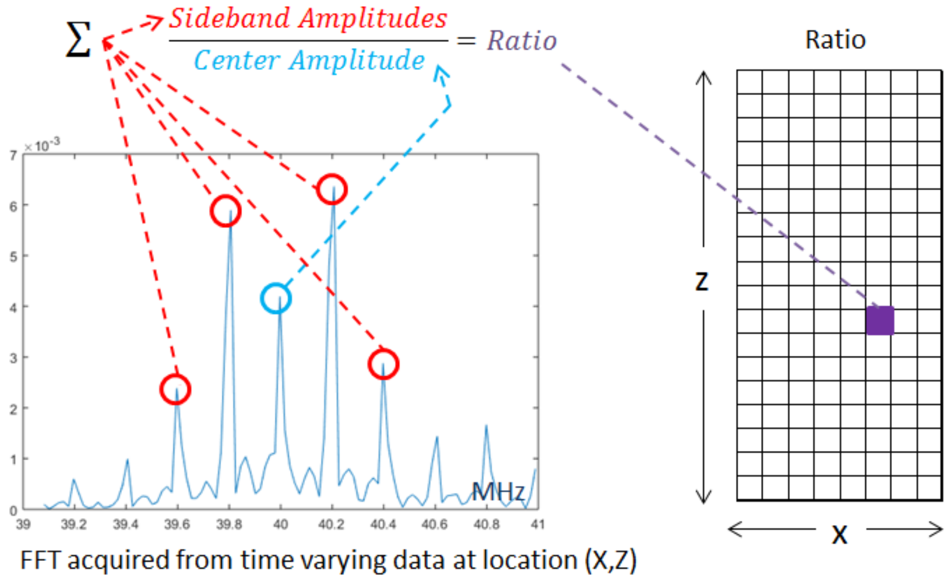

Figure 7.4.12 - *Ratio Method*

Figure 7.4.13 – *Ratio of Amplitudes*

Sideband amplitudes were observed to be more pronounced later into the plasma afterglow at specific locations within the plane of measurement. The locations where the ratios are observed to be higher grow into a relatively fixed location within the plane of measurement for the $Bx_{(x,z)}$, $By_{(x,z)}$ components. Locations where the $Bz_{(x,z)}$ ratios are relatively larger appear nearer to the loop antenna in the early afterglow, then move away from the loop antenna to rest at a fixed location as time progresses. Figure 7.4.14 imposes the locations where the LOR should exist given the parameters in Table 7.1. There appears to be some correlation of the locations of the where higher sideband amplitudes exist, and the locations of the LOR.

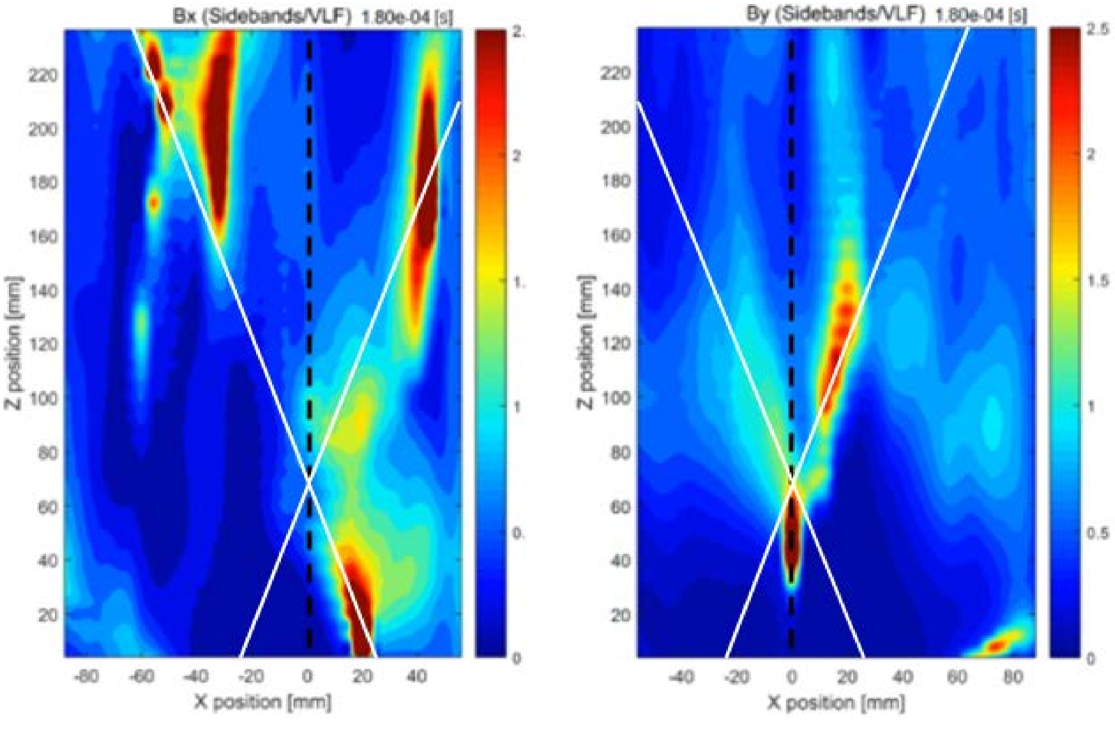

Figure 7.4.14 – *White line display the locations where the resonance cones are expected to exist given the experimental parameters*

8 Conclusion

Previous theoretical work has outlined a novel method for efficient generation of electromagnetic VLF waves in cold magnetized plasmas. This novel method, a parametric antenna, has the potential to make satellite based large scale radiation belt remediation a reality.

The efforts of this project can be summarized as follows. A scaled ionospheric plasma simulation chamber was constructed to perform extensive experiments which examined VLF and IA wave propagation from a loop and mesh antenna for their non-linear interaction. These experiments served to verify the theory by showing large portions of wave amplitude existing in mixed mode frequencies.

The total sum of this effort has increased the readiness of this technology from a basic theoretical design to bench level demonstrations in a relevant environment supported by experimental data. However, there is still much future work to be performed to make this method of radiation belt remediation a reality.

9 Bibliography

[1] T. Bell and T. Wang, "Radiation resistance of a small filamentary loop antenna in a cold multicomponent magnetoplasma," vol. 4, no. AP-19, 1971.

[2] J. Chugunov, ""Electric Characteristic of magnetic type exciters in plasma," *Sov. Izv. Vuzov. Radiotechn. Electron*, p. 18.6, 1973.

[3] L. F. a. N. Marcuvitz, Radiation and Scattering of Waves, Pretence Hall, 1973.

[4] G. Golubyatnikov, "Excitation of Electrostatic and Whistler Waves by a Magnetic Type Antenna," *Sov. Phys. J. Exp. Theor. Phys*, pp. 94, 124, 1988.

[5] V. Karpman, "Fizika Plasmy 12," 1986.

[6] V. Karpman, "Reasonance Cones of a Magnetic Ring Antenna in an Anisotropic Plasma," *Physics Letters A,* vol. 117, no. 2, pp. 73-76, 1986.

[7] V. Sotnikov, G. Solovyev, M. Ashour-Abdalla, D. Shriver and V. Fiala, "Structure of the near zone electric field and the power radiated from a VLF antenna in the ionosphere," *Radio Science*, vol. 28, no. 6, pp. 1087-1103, November 1993.

[8] P. Triska and V. I. Shevchenko, ""Active" project satellites," in *XXVIII Committee on Space Research*, The Hague, 1990.

[9] R. K. Fisher and R. W. Gould, "Resonance Cones in the Field Pattern of a Radio Frequency Probe in a Warm Anisotropic Plasma," *The Physics of Fluids,* vol. 14, no. 4, pp. 857-867, April 1971.

[10] J. M. Urrutia and R. L. Stenzel, "Magnetic Antenna exciation of whistler modes. 1. Basic Properties," 2014.

[11] T. N. C. Wang and T. F. Bell, "VLF/ELF Radiation Patterns of Arbitrarily Orientated Electric and Magnetic Dipoles in a Cold Lossless Multicomponent Magnetoplasma," *Journal of Geophysical Research,* vol. 77, no. 7, pp. 1174-1189, March 1972.

[12] V. Sotnikov, Structure of the Near Zone Electric Field and the Power Radiated from a VLF Antenna in the Ionosphere, Radio Science, Vol.28, No.6, pp.1087-1103, 1993.

[13] C. K. Birdsall and A. B. Langdon, Plasma Physics via Computer Simulation, New York, New York: Taylor and Francis Group, 2005, pp. 369-370.

[14] R. Z. Sagdeev, V. I. Sotnikov, V. D. Shapiro and V. I. Shevchenko, "Contribution to the theory of magnetosonic turbulence," *JETP Lett.*, pp. Vol. 26, No. 11, P. 582, 1977.

[15] V.Sotnikov, "Private communications with Sotnikov," 2014.

[16] P. Kulkarni, U. S. Inan, T. F. Bell and J. Bortnik, "Precipitation signatures of ground-based VLF transmitters," *J. Geophys.*, vol. 113, p. A07214, 2008.

[17] M. Balkey, "Optimization of a Helicon Plasma Source for Maximum Density with Minimal Ion Heating," *Dissertation Abstracts International,* vol. 62, no. 4, 2000.

[18] J. Huba, NRL Plasma Formulary 2016, Washington, DC, 2016.

[19] F. Chen, Permanent-magnet helicon sources and arrays: a new type of rf plasma, Los Angeles, California: Phys. Plasmas 16, 057102 (2009), May 18, 2009.

[20] W. Gekelman, "Ion acoustic wave experiments in a high school plasma physics laboratory," *American Journal of Physics,* vol. 75, no. 2, pp. 103-110, 2007.

[21] F. Chen, Langmuir Probe Diagnostics, Jeju Korea: IEEE-ICOPS meeting, June 5, 2003.

[22] I. Sudit, RF Compensated Probes for High-Density Discharges, Los Angeles: Plasma Sources Sci. Technol.3, Nov.1993.

[23] D.Trunec, P.Spanel and D.Smith, "Electron Temperature Relaxation in Afterglow Plasmas," *Contributions to Plasma Physics*, vol. 34, pp. 69-79, 1994.

[24] R. Stenzel and W.Gekelman, "Nonlinear interactions of focused resonance cone fields with plasmas," *Physics of Fluids,* vol. 20, pp. 108-115, 1977.

[25] M. Urrutia, "Magnetic Antenna Excitation of Whistler Modes. I. Basic Properties," *Physics of Plasmas*, vol. 21, 2014.